The Astrophysical Journal, 776:1 (20pp), 2013 October 10 doi:10.1088/0004-637X/776/1/1

THREE-DIMENSIONAL HYDRODYNAMIC SIMULATIONS OF MULTIPHASE GALACTIC DISKS WITH STAR FORMATION FEEDBACK. I. REGULATION OF STAR FORMATION RATES

Chang-Goo Kim[1], Eve C. Ostriker[2,3], and Woong-Tae Kim[4]
[1] Department of Physics and Astronomy, University of Western Ontario, London, Ontario N6A 3K7, Canada; ckim256@uwo.ca
[2] Department of Astronomy, University of Maryland, College Park, MD 20742, USA; eco@astro.princeton.edu
[3] Department of Astrophysical Sciences, Princeton University, Princeton, NJ 08544, USA
[4] Center for the Exploration of the Origin of the Universe (CEOU), Astronomy Program, Department of Physics and Astronomy, Seoul National University, Seoul 151-742, Korea; wkim@astro.snu.ac.kr
Received 2013 May 14; accepted 2013 August 13; published 2013 September 17

ABSTRACT

The energy and momentum feedback from young stars has a profound impact on the interstellar medium (ISM), including heating and driving turbulence in the neutral gas that fuels future star formation. Recent theory has argued that this leads to a quasi-equilibrium self-regulated state, and for outer atomic-dominated disks results in the surface density of star formation $\Sigma_{\rm SFR}$ varying approximately linearly with the weight of the ISM (or midplane turbulent + thermal pressure). We use three-dimensional numerical hydrodynamic simulations to test the theoretical predictions for thermal, turbulent, and vertical dynamical equilibrium, and the implied functional dependence of $\Sigma_{\rm SFR}$ on local disk properties. Our models demonstrate that all equilibria are established rapidly, and that the expected proportionalities between mean thermal and turbulent pressures and $\Sigma_{\rm SFR}$ apply. For outer disk regions, this results in $\Sigma_{\rm SFR} \propto \Sigma\sqrt{\rho_{\rm sd}}$, where Σ is the total gas surface density and $\rho_{\rm sd}$ is the midplane density of the stellar disk (plus dark matter). This scaling law arises because $\rho_{\rm sd}$ sets the vertical dynamical time in our models (and outer disk regions generally). The coefficient in the star formation law varies inversely with the specific energy and momentum yield from massive stars. We find proportions of warm and cold atomic gas, turbulent-to-thermal pressure, and mean velocity dispersions that are consistent with solar-neighborhood and other outer disk observations. This study confirms the conclusions of a previous set of simulations, which incorporated the same physics treatment but was restricted to radial-vertical slices through the ISM.

Key words: galaxies: ISM – galaxies: kinematics and dynamics – galaxies: star formation – methods: numerical – turbulence

Online-only material: color figures

1. INTRODUCTION

Disk galaxies like the Milky Way are long-lived systems, evolving (in the absence of interactions) only on timescales of several orbits. The interstellar medium (ISM) also evolves slowly overall, such that there are well-defined ISM properties when averaged over a spatial domain of several disk scale heights and several tenths of an orbit. On small spatial scales, however, the ISM is highly structured, and can change rapidly as both thermal and dynamical timescales are short. These short timescales suggest that the ISM will be able to evolve to a quasi-equilibrium state, in which heating balances cooling, and in which the mean pressure in the diffuse gas at any height balances the weight of the overlying ISM. The ideas that thermal and vertical "hydrostatic" equilibrium should approximately apply are widely held (see, e.g., the reviews of Ferrière 2001; Cox 2005) and have been studied in detail over many decades in the astrophysical literature. Turbulence has only been studied more recently with the advent of numerical hydrodynamic simulations, but it too is expected to reach an equilibrium between driving and dissipation (cf. Stone et al. 1998; Mac Low 1999). Although thermal pressure plays a role, turbulent pressure is believed to be the most important contributor to vertical force balance in the atomic ISM (Lockman & Gehman 1991).

In models of the atomic ISM, the heating rate per particle, and therefore the equilibrium thermal pressure, is generally treated as an independent parameter, set based on empirical values of ambient UV, X-rays, and cosmic rays, with far-UV (FUV) from young stars the dominant term (e.g., Wolfire et al. 1995, 2003). Many processes may contribute to turbulent driving (e.g., Elmegreen & Scalo 2004), but those associated with feedback from young stars are likely to be the most important on scales relevant for vertical dynamical equilibrium within the disk. Similar to the case for thermal pressure, empirical measures of the supernova (SN) rate have often been used to obtain predictions for the turbulent pressure in ISM models (e.g., McKee & Ostriker 1977).

For a self-consistent ISM model, the equilibrium pressure obtained by balancing various gain and loss terms must be the same as the equilibrium pressure that offsets the vertical weight of the gas. Ostriker et al. (2010, hereafter OML10) and Ostriker & Shetty (2011, hereafter OS11) used this principle, in combination with relations between turbulent and thermal driving and the star formation rate (SFR), to obtain predictions for the equilibrium SFR in disk systems regulated by feedback. In this model framework, the radiation fields and SN rates that control thermal and turbulent pressure in the ISM are no longer considered independent (or empirically determined) parameters, but must evolve (together with an evolving SFR) to levels that yield pressures that are consistent with vertical dynamical equilibrium.

Kim et al. (2011, hereafter Paper I) tested this feedback-regulated simultaneous equilibrium model via numerical hydrodynamic simulations for the outer disk regime in which gas is primarily atomic (both warm and cold), while Shetty & Ostriker

(2012, hereafter SO12) tested the equilibrium model with simulations of the starburst regime in which gas is mainly molecular and cold. Both of these numerical studies demonstrated that models for a wide range of parameters indeed evolve to a quasi-steady, turbulent state. Key physical quantities, such as the SFR surface density ($\Sigma_{\rm SFR}$), disk scale height, midplane thermal and turbulent pressures, warm and cold gas fractions, and mass-weighted velocity dispersions, reach well-defined mean values within an orbital time. The saturation of these statistical properties enables a comparison with the theory of self-regulated star formation developed in OML10 and OS11, and also provides calibrations of certain parameters that enter the theory.

In this paper, we return to the atomic-dominated outer disk regime, but extend the simulations of Paper I from two-dimensional radial-vertical domains to fully three-dimensional (3D) models. We explore a wide range of total gas surface density $\Sigma \sim 2.5$–$20\,M_\odot\,{\rm pc}^{-2}$ and midplane density of stars plus dark matter $\rho_{\rm sd} \sim 0.003$–$0.45\,M_\odot\,{\rm pc}^{-3}$. We also include sheared galactic rotation, focusing on model families in which the angular speed $\Omega \propto \Sigma$ so that the Toomre parameter in the gas is constant ($Q \sim 2$ for saturated-state turbulence velocity dispersion $\sim 7\,{\rm km\,s}^{-1}$). Our feedback prescription includes both time-dependent heating and turbulent driving dependent on the SFR, as described in Section 2.1. We also vary the heating efficiency $f_{\rm rad} \sim 0.2$–5 that connects the heating rate and the SFR surface density. This allows us to explore how, e.g., varying dust abundance (which would alter radiation penetration and heating) may affect the saturated state and evolution.

As we shall describe, our simulations show that realistic SFRs are obtained when momentum feedback at the levels expected from the corresponding Type II SN rates are included. This affirms the conclusions reached in our previous numerical studies (Paper I; SO12). Although detailed prescriptions differ, recent work from other groups has reached similar conclusions regarding the ability of sufficient momentum feedback to self-regulate star formation at realistic levels (e.g., Dobbs et al. 2011; Hopkins et al. 2011; Agertz et al. 2013). Beyond simply demonstrating that feedback is effective in self-regulating star formation, we also show (following Paper I) that SFRs obey a near-linear scaling with the pressure of the diffuse ISM, and we relate the coefficient to the inverse of the specific momentum injected by massive stars. This explains empirical correlations of molecular gas and star formation with pressure identified by Blitz & Rosolowsky (2004, 2006) and Leroy et al. (2008). Our numerical results confirm the conclusion of Paper I that both warm and cold atomic gas are expected to be present in the ISM for a wide range of conditions, consistent with observations of both the solar-neighborhood (Heiles & Troland 2003) and distant outer disk regions (Dickey et al. 2009; Pineda et al. 2013) of the Milky Way.

The plan of this paper is as follows. In Section 2, we summarize our numerical methods and the parameter sets chosen for our simulations modeling varying galactic environments. In Section 3, we present our results, including an overview of evolution (Section 3.1), statistics of saturated-state properties for different models (Section 3.2), comparison with the predictions for vertical dynamical, thermal, and turbulent equilibrium based on these statistics (Section 3.3), and comparison with the theoretical predictions for equilibrium star formation scalings and rates (Section 3.4). We summarize and discuss our main conclusions in Section 4.

2. NUMERICAL METHODS AND MODELS

2.1. Numerical Methods

We consider local "shearing box" models of galactic disks in three dimensions (e.g., Kim et al. 2002, 2003). The axes in the local Cartesian frame are $x \equiv R - R_0$ and $y \equiv R_0(\phi - \Omega t)$, where R_0 is the galactocentric radius at the center of the domain and $\Omega \equiv \Omega(R_0)$ is the angular velocity at R_0; z is the vertical coordinate centered on the galactic midplane. The background velocity in this local frame relative to the domain center (at $x = y = z = 0$) has the form $\mathbf{v}_0 = -q\Omega x\hat{\mathbf{y}}$, where $q \equiv -(d\ln\Omega/d\ln R)|_{R_0}$ is the local shear rate. We assume a flat rotation curve, such that we set $q = 1$ and the local epicyclic frequency is $\kappa = \sqrt{2}\Omega$. The shearing box formulation in the local frame includes tidal gravity and Coriolis force terms in the horizontal direction. In addition, we include a (fixed) vertical gravitational potential to model the stellar disk and dark matter halo, self-gravity of gas, cooling and heating, and thermal conduction. The resulting set of equations (see, e.g., Piontek & Ostriker 2007; Paper I) is

$$\frac{\partial\rho}{\partial t} + \nabla\cdot(\rho\mathbf{v}) = 0, \tag{1}$$

$$\frac{\partial\mathbf{v}}{\partial t} + \mathbf{v}\cdot\nabla\mathbf{v} = -\frac{1}{\rho}\nabla P - 2\boldsymbol{\Omega}\times\mathbf{v} + 2q\Omega^2 x\hat{\mathbf{x}} - \nabla\Phi + \mathbf{g}_{\rm sd}, \tag{2}$$

$$\frac{\partial e}{\partial t} + \nabla\cdot(e\mathbf{v}) = -P\nabla\cdot\mathbf{v} - \rho\mathcal{L} + \mathcal{K}\nabla^2 T, \tag{3}$$

$$\nabla^2\Phi = 4\pi G\rho, \tag{4}$$

where $\mathbf{g}_{\rm sd}$ is the external gravity, $\rho\mathcal{L}$ is the net cooling rate per unit volume, and $\mathcal{K} = 4\times10^7\,{\rm erg\,s^{-1}\,cm^{-1}\,K^{-1}}/[1 + (0.05\,{\rm cm}^{-3}/n)]$ is the conductivity adopted such that thermal instability is resolved on our grid (Koyama & Ostriker 2009a; Paper I). Other symbols have their usual meanings. We assume that the gas has cosmic abundance so that the gas pressure is $P = 1.1nk_{\rm B}T$, where $n = \rho/(1.4m_p)$ is the number density of hydrogen nuclei. An ideal gas law is assumed with internal energy density $e = (3/2)P$.

Since the vertical gradient scales of stellar disks and dark matter halos are generally much larger than those of gaseous disks (and vertical domain sizes in our simulations), we adopt the simple approach of taking external gravity as a linear function of the vertical coordinate z:

$$\mathbf{g}_{\rm sd} = -4\pi G\rho_{\rm sd} z\hat{\mathbf{z}}, \tag{5}$$

where $\rho_{\rm sd}$ is the stellar *plus* dark matter volume density at the midplane.

The net volumetric cooling function is given by $\rho\mathcal{L} \equiv n[n\Lambda(T) - \Gamma]$. For the diffuse ISM, radiative cooling by the C II 158 μm fine-structure line and by Lyα line emission is dominant at low and high temperature, respectively, whereas grain photoelectric heating by FUV radiation with energy $6\,{\rm eV} < h\nu < 13.6\,{\rm eV}$ is dominant in both the cold and warm phases (Bakes & Tielens 1994). We adopt the fitting formula for the cooling function from Koyama & Inutsuka (2002):

$$\Lambda(T) = 2\times10^{-19}\exp\left(\frac{-1.184\times10^5}{T+1000}\right) + 2.8\times10^{-28}\sqrt{T}\exp\left(\frac{-92}{T}\right)\ {\rm erg\,cm^3\,s^{-1}}, \tag{6}$$

with temperature T in degrees Kelvin.

We adopt the same star formation feedback prescription as in Paper I. This includes momentum feedback (to represent the radiative stage of blasts produced by SN explosions) at a rate proportional to the SFR, together with a time-dependent heating rate that is also proportional to the SFR (representing radiative heating from young, massive stars). We scale the heating rate relative to the fiducial solar-neighborhood value adopted by Koyama & Inutsuka (2002), $\Gamma_0 = 2\times10^{-26}$ erg s^{-1} (see below).

The reader is referred to Paper I for a full description of the feedback prescription. Here we only give a brief summary. Star formation is taken to occur only when the density of the grid zone exceeds a threshold[5] $n_{\rm cr} = 200\,{\rm cm}^{-3}\,(\Gamma/\Gamma_0)^{0.2}$. The probability of massive star formation in a given zone with simulation time step Δt is

$$\mathcal{P}_* = \frac{\dot{M}_*}{m_*}\Delta t, \tag{7}$$

where $\dot{M}_*$ is the expected SFR for a given grid zone, and $m_* = 100\,M_\odot$ represents the total mass in stars (averaged over the initial mass function) per SN (cf., Kroupa 2001). The expected SFR for a grid zone with density $\rho > \rho_{\rm cr}$ is taken as

$$\dot{M}_* = \dot{\rho}_*\Delta V = \epsilon_{\rm ff}\frac{\rho\Delta V}{t_{\rm ff}(\rho)}, \tag{8}$$

where $\Delta V = \Delta x\Delta y\Delta z = (2\,{\rm pc})^3$ is the volume element of the grid zone, $\epsilon_{\rm ff}$ is the star formation efficiency per free-fall time of dense, self-gravitating gas, and $t_{\rm ff}(\rho) \equiv [3\pi/(32G\rho)]^{1/2}$ is the free-fall time of a given grid zone. We take a fiducial value $\epsilon_{\rm ff} = 0.01$, which is consistent with theory and observations of dense ISM gas (Krumholz & McKee 2005; Krumholz & Tan 2007; Krumholz et al. 2012). We note that based on the study of SO12, the adopted value of $\epsilon_{\rm ff}$ can be varied by an order of magnitude with little effect on the resulting mean SFR, provided that the threshold density is sufficiently high compared to the mean value in the diffuse ISM.

When a massive star forms, we immediately apply momentum feedback in its vicinity, i.e., we neglect time delays (see below and Paper I). For each feedback event, we first take spatial averages within a sphere of radius $r_{\rm sh}$ and redistribute mass, momentum, and thermal energy with their respective averaged values. We adopt a fixed value $r_{\rm sh} = 10\,{\rm pc}$ as representative of the shell formation epoch (Cioffi et al. 1988; Koo & Kang 2004). We then add to the local momentum density a quantity with a form $\rho\mathbf{v}(\mathbf{r}) = p_{\rm sh}(r/r_{\rm sh})^2\hat{\mathbf{r}}$, where $\mathbf{r}$ is the position vector measured from the center of the SN feedback region, and $p_{\rm sh} = 5p_*/(4\pi r_{\rm sh}^3)$ is the momentum density at $r = r_{\rm sh}$. This injects a total radial momentum p_* to the surrounding medium; physically, p_* represents the value of the shell momentum in the radiative stage of a SN remnant. Thornton et al. (1998) studied the evolution of expanding spherical SN remnants with realistic radiative cooling and found that the shell momentum is $p_* \sim (1\text{–}4)\times10^5\,M_\odot\,{\rm km\,s^{-1}}$ at the time of maximum luminosity and a factor ~2.5 larger after shell cooling has declined, with the highest values corresponding to low metallicity. The simulations of Cioffi et al. (1988) and Blondin et al. (1998) found similar values at solar metallicity. In the present work, we adopt $p_* = 3\times10^5\,M_\odot\,{\rm km\,s^{-1}}$. For uniform-density conditions, there is only a weak dependence of the radiative-stage momentum on the ambient density ($p_* \propto \bar{n}^{-0.12}$), because momentum in the Sedov stage varies as $\sim E_{\rm SN}/v_{\rm shock}$ and the onset of the radiative stage is the point at which $v_{\rm shock}$ drops enough that post-shock cooling becomes strong (see, e.g., the physical discussion in Blondin et al. 1998). For a strongly clumped medium, however, both the radius at the radiative stage and the net momentum injection may depart more strongly from our adopted value; this will be evaluated with future simulations.

For radiative feedback, we count the number of recent massive star formation events over $t_{\rm bin}$ to calculate the recent SFR:

$$\Sigma_{\rm SFR} = \frac{\mathcal{N}_* m_*}{L_x L_y t_{\rm bin}}, \tag{9}$$

where $\mathcal{N}_*$ stands for the total number of massive stars formed during the time interval $(t - t_{\rm bin},\, t)$. In contrast to Paper I, our simulation domain is sufficiently large in the azimuthal direction so that $t_{\rm bin}$ can be set to the realistic lifetime of OB stars, $t_{\rm FUV} = 10\,{\rm Myr}$ (Parravano et al. 2003).[6] We assume a simple linear relationship between the heating rate Γ, the mean FUV radiation field $J_{\rm FUV}$, and the SFR surface density $\Sigma_{\rm SFR}$ (see OML10; Paper I) normalized relative to solar-neighborhood conditions, such that

$$\Gamma = \Gamma_0\left[f_{\rm rad}\left(\frac{\Sigma_{\rm SFR}}{\Sigma_{\rm SFR,0}}\right) + \left(\frac{J_{\rm FUV,meta}}{J_{\rm FUV,0}}\right)\right]. \tag{10}$$

In Equation (10), we adopt the solar-neighborhood fiducial heating rate $\Gamma_0 = 2\times10^{-26}\,{\rm erg\,s^{-1}}$ from Koyama & Inutsuka (2002), the SFR surface density in the solar neighborhood $\Sigma_{\rm SFR,0} = 2.5\times10^{-3}\,M_\odot\,{\rm kpc^{-2}\,yr^{-1}}$ from Fuchs et al. (2009), and $J_{\rm FUV,meta} = 0.0024\,J_{\rm FUV,0}$ to represent the metagalactic FUV radiation field (Sternberg et al. 2002). As in Paper I, we introduce a parameter $f_{\rm rad}$ to allow for variable heating efficiency at a given SFR relative to our adopted parameters. By increasing/decreasing $f_{\rm rad}$, we can also represent greater/lesser penetration of FUV through the ISM as would occur for lower/higher dust abundance.

We utilize the Athena code with the van Leer integrator (Stone & Gardiner 2009), Roe's Riemann solver, a piecewise linear spatial reconstruction scheme, and the orbital advection method for a shearing box (Stone & Gardiner 2010). In addition, we adopt a fast Fourier transform Poisson solver method with treatment of shearing horizontal coordinates as introduced by Gammie (2001) and with vacuum vertical boundary conditions as introduced by Koyama & Ostriker (2009a). We include cooling/heating and thermal conduction terms in an operator split manner. For the net cooling, we use an implicit solution method based on Simpson's rule and apply subcycling to limit the maximum temperature change to <50% of previous value over all grid zones. If the change of temperature exceeds 50% of the previous value, we halve the timestep and repeat subcycles for the specific grid zone until the temperature change for one hydrodynamic timestep update is smaller than 50%.

Similar to Paper I, we mention several caveats regarding the current simulations. First, the feedback from SN explosions is

[5] The threshold density is calculated based on the thermal equilibrium state of cold gas, $n_{\rm cr} = \Gamma/\Lambda(T_{\rm cr})$, where $T_{\rm cr}$ is the threshold temperature. For our net cooling function, the Jeans length is $\lambda_J \approx 1.4T_{\rm cr}^{3/4}e^{-46/T_{\rm cr}}(\Gamma/\Gamma_0)^{-1/2}$ pc (Paper I). By taking $\lambda_J = 5$ pc, $T_{\rm cr}$ (and hence $n_{\rm cr}$) can be found as a function of Γ/Γ_0. Using a power-law fit, we obtain $n_{\rm cr}$ given in the main text, representing the maximum density for which the Jeans length is well resolved (cf. Truelove et al. 1997) at our adopted spatial resolution of 2 pc.

[6] For the QA02 model, which has extremely low surface density, we adopt $t_{\rm bin} = 40\,{\rm Myr}$ to partly compensate for the fact that the domain of influence of FUV radiation would be approximately four times larger than the horizontal area of our simulation box. Note that this time is still very short compared to the orbit time $t_{\rm orb}$ and the vertical oscillation period $t_{\rm osc}$ for the QA02 model. Also, for 3DS and XZ models with smaller azimuthal domain size (see Section 2.2), we extend $t_{\rm bin}$ to $0.5t_{\rm orb}$.

realized solely via expanding SN remnants rather than injecting thermal energy, which would create a hot ISM (McKee & Ostriker 1977). More realistically, the hot ISM would occupy a significant volume even near the midplane (e.g., Hill et al. 2012), together with the cold and warm phases in approximate pressure equilibrium. Due to its large-scale height, however, most of the hot gas does not participate in supporting the weight of the warm/cold diffuse gas, although expansion of highly overpressured hot SN remnants is crucial in driving turbulence within the surrounding warm/cold ISM; we model the latter effect. Based on our conclusion that the SFR is regulated by midplane total pressure (Section 3.4), we believe that our main findings are robust, in spite of our simplified treatment of SNe. We note that using preliminary simulations in which SNe are modeled with thermal energy input (rather than momentum input), we recover similar results for SFRs to those reported here.

A second caveat is that the feedback we apply is instantaneous, whereas a more realistic treatment of stellar evolution would include inputs from stellar winds and expanding H II regions (e.g., Mac Low & Klessen 2004) prior to SN explosions. Since SNe are the most powerful driving source of turbulence averaged over the ISM (p_*/m_* for stellar winds and expanding H II regions would be an order of magnitude lower than that of SNe; see OS11), we believe that the current simplified approach is an adequate first approximation for modeling SFR self-regulation in diffuse-dominated regions. Feedback from earlier stages of massive star evolution would, however, affect the detailed properties and lifetimes of gravitationally bound clouds (GBCs), so including these effects will be important in modeling higher-Σ galactic regions where most of the ISM mass is in GBCs rather than diffuse structures. For this reason, we confine ourselves here to the regime $\Sigma \leqslant 20\,M_\odot\,\mathrm{pc}^{-2}$ in which the observed ISM is predominantly in the diffuse atomic component. When spiral arms or bars are taken into account, the time delay between the epochs of star formation and feedback would likely also be important (e.g., Kim et al. 2010; Seo & Kim 2013).

2.2. Model Parameters

We run the same set of models as in Paper I, which covers a wide range of outer disk conditions for nearby galaxies. Our parameters are the gas surface density Σ, the stellar plus dark matter density at the midplane $\rho_{\rm sd}$, and the galactic rotational speed Ω. We have five model series: QA, QB, S, G, and R. For all series, the angular speed of galactic rotation varies as $\Omega = 28\,\mathrm{km\,s^{-1}\,kpc^{-1}}(\Sigma/10\,M_\odot\,\mathrm{pc}^{-2})$, such that the gaseous Toomre stability parameter $Q_g \equiv \kappa\sigma_x/(\pi G\Sigma)$ would be constant for fixed radial ($\hat{x}$) gas velocity dispersion σ_x ($Q_g \sim 2$ for $\sigma_x = 7\,\mathrm{km\,s^{-1}}$). In the QA and QB series, $\rho_{\rm sd} \propto \Sigma^2$ such that the stellar Toomre parameter would also be constant within each series. These two series differ only in the ratio of self-to-external (i.e., gaseous-to-stellar+dark matter) gravity: $s_0 = 0.28$ and 0.07 for the QA and QB series, respectively, where $s_0 \equiv \pi G\Sigma^2/(2\sigma_z^2\rho_{\rm sd})$ (cf., Kim et al. 2002). The QA and QB series may thus each be thought of as representing a sequence of radii in a $Q_g = $ const, $Q_* = $ const galaxy, where the stellar disk is a factor of four more massive in the QB series than in the QA series. For the S series we fix $\rho_{\rm sd}$ and vary Σ, whereas for the G series we fix Σ and vary $\rho_{\rm sd}$. For the R series, we vary $f_{\rm rad}$ for the fiducial model QA10, to test the effect of varying the heating efficiency or dust shielding for FUV. We list the model parameters in Table 1. In all models, the orbital period is $t_{\rm orb} = 2\pi/\Omega = 220\,\mathrm{Myr}\,(\Omega/28\,\mathrm{km\,s^{-1}\,kpc^{-1}})^{-1} = 220\,\mathrm{Myr}\,(\Sigma/10\,M_\odot\,\mathrm{pc}^{-2})^{-1}$, which we take as the time unit in our presentation.

Table 1
Model Parameters

Model	Σ ($M_\odot$ pc^{-2})	$\rho_{\rm sd}$ ($M_\odot$ pc^{-3})	$t_{\rm orb}$ (Myr)	L_z (pc)	s_0	$f_{\rm rad}$
QA02	2.5	0.0031	878	2048	0.28	1.0
QA05	5.0	0.0125	439	1024	0.28	1.0
QA07	7.5	0.0281	293	768	0.28	1.0
QA10	10.0	0.0500	219	512	0.28	1.0
QA15	15.0	0.1125	146	384	0.28	1.0
QA20	20.0	0.2000	110	256	0.28	1.0
QB02	2.5	0.0125	878	1024	0.07	1.0
QB05	5.0	0.0500	439	768	0.07	1.0
QB07	7.5	0.1125	293	512	0.07	1.0
QB10	10.0	0.2000	219	384	0.07	1.0
QB15	15.0	0.4500	146	256	0.07	1.0
S02	2.5	0.0500	878	1024	0.02	1.0
S07	7.5	0.0500	293	768	0.16	1.0
S15	15.0	0.0500	146	512	0.62	1.0
S20	20.0	0.0500	110	512	1.10	1.0
G01	10.0	0.0125	219	1024	1.10	1.0
G02	10.0	0.0250	219	768	0.55	1.0
G10	10.0	0.1000	219	512	0.14	1.0
G40	10.0	0.4000	219	384	0.03	1.0
R02	10.0	0.0500	28	512	0.28	0.2
R05	10.0	0.0500	28	512	0.28	0.5
R25	10.0	0.0500	28	512	0.28	2.5
R50	10.0	0.0500	28	512	0.28	5.0

Notes. Physical input parameters are the same as in Paper I. Full 3D simulations with $L_x = L_y = 512\,\mathrm{pc}$ are run only for models QA02, QA05, QA10, QA20, and R50 (bold face in first column). "Slim" 3D simulations ($L_x = 512\,\mathrm{pc}$, $L_y = 32\,\mathrm{pc}$) are run for all parameters.

We take $L_x = 512\,\mathrm{pc}$ and $L_z = 4H_w$ for the horizontal and vertical domain sizes. Here $H_w \equiv c_w/(4\pi G\rho_{\rm sd})^{1/2}$ is a nominal Gaussian scale height of warm gas with $c_w = 7\,\mathrm{km\,s^{-1}}$, which varies from model to model. In all models, we vary the number of grid zones such that the grid resolution[7] is $\Delta x = \Delta y = \Delta z = 2$ pc. In the azimuthal direction, we consider two different domain sizes: one set is full 3D simulations using azimuthal domain size $L_y = L_x = 512$ pc (hereafter 3DF models), and the other set uses a slimmer azimuthal domain size $L_y = 32$ pc (hereafter 3DS models). Since full 3D simulations require considerable computational resources, it is impractical to run 3DF models for all parameter values. Our 3DS models cover the whole parameter space, while the 3DF models cover just the QA and R series (see Table 1). In forthcoming sections, we shall show that 3DF and 3DS models yield essentially the same results in terms of statistical properties at saturation. We also compare these properties to the results from the simulations of Paper I, which followed the evolution of two-dimensional radial-vertical slices through the disk; these are denoted as "XZ" models. In the remainder of this paper, we use suffixes 3DF, 3DS, and XZ to distinguish models with the same parameters but different azimuthal domain size. The term "3D models" denotes both 3DF and 3DS models.

[7] Although the resolution is a factor of two lower than in Paper I, we have confirmed that the key physical properties are converged even at lower resolution than we adopt here.

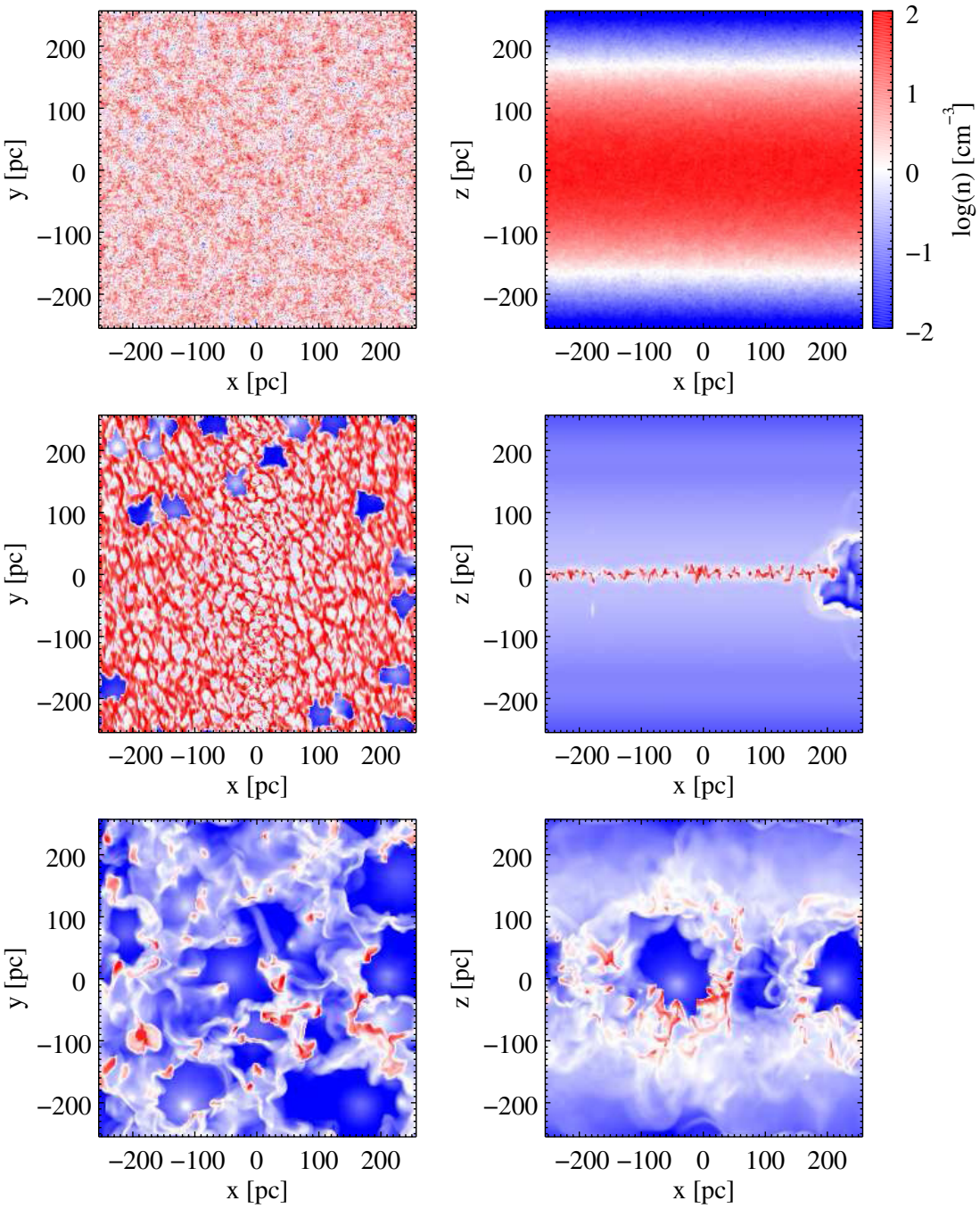

Figure 1. Snapshots of density in the solar-neighborhood-like model QA10-3DF (logarithmic color scale) at early evolutionary stages, $t/t_{\rm orb} = 0$ (top), 0.1 (middle), and 0.2 (bottom). The left and right columns display horizontal and vertical slices through the computational domain at $z = 0$ and $y = 0$, respectively. The initial disk rapidly separates into two phases due to thermal instability, with the cold gas settling to the midplane (Kim et al. 2010). Gravity causes the cold gas to collect into GBCs where star formation occurs, and produces feedback, starting at $t/t_{\rm orb} = 0.1$ (middle row). Energy injected by SNe drives turbulence, expanding the disk vertically (see evolution from middle right to lower right) and helping to create large-scale clumpy/filamentary structure.

(A color version of this figure is available in the online journal.)

3. SIMULATION RESULTS

3.1. Overview of Time Evolution and Disk Properties

In this subsection, we describe details of time evolution and properties of our disk models. We begin with our fiducial model, QA10, which adopts $\Sigma = 10\,M_\odot\,{\rm pc}^{-2}$, $\rho_{\rm sd} = 0.05\,M_\odot\,{\rm pc}^{-3}$, and $\Omega = 28\,{\rm km\,s^{-1}\,kpc^{-1}}$, similar to conditions in the solar neighborhood. Figure 1 shows evolving density slices of the QA10-3DF model in the horizontal *XY*-plane (at the disk midplane $z = 0$; left) and radial-vertical *XZ*-plane ($y = 0$; right) at $t/t_{\rm orb} = 0$ (top), 0.1 (middle), and 0.2 (bottom). The initial gas distribution (top row of Figure 1) follows a Gaussian vertical density profile with scale height of ∼80 pc. In the initial conditions, we impose a Gaussian random density perturbation with flat spectrum at wavenumbers smaller than $kL_z/2\pi = 8$ and total amplitude of 10%. This choice of initial conditions allows rapid growth of thermal instability near the midplane, evolving toward two-phase thermal equilibrium (see

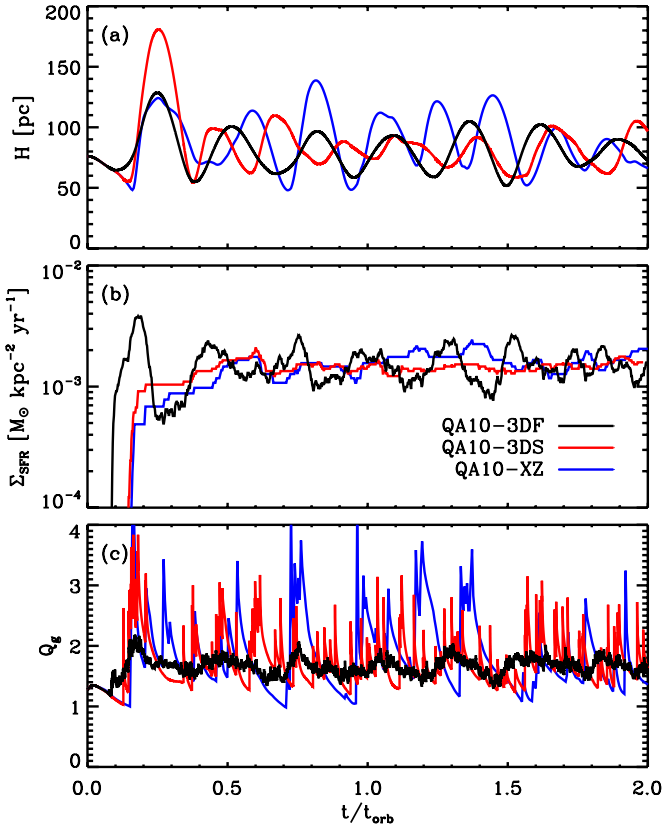

Figure 2. Time evolution of (a) the density-weighted vertical scale height H, (b) the SFR surface density Σ_{SFR}, and (c) the gaseous Toomre stability parameter Q_g for models QA10-3DF (black), QA10-3DS (red), and QA10-XZ (blue). These models differ only in their azimuthal domain sizes. The evolution is similar for all models. The temporal fluctuations in Σ_{SFR} are smeared out in models QA10-3DS and QA10-XZ due to the larger binning adopted for Σ_{SFR} (see text). The temporal fluctuations in Q_g are smeared out in model QA10-3DF due to a much larger averaging volume compared to models QA10-3DS and QA10-XZ. The mean values of $H \sim 80$ pc, $\Sigma_{SFR} \sim 1.5 \times 10^{-3}\, M_\odot$ kpc^{-2} yr^{-1}, and $Q_g \sim 1.7$ after saturation ($t/t_{orb} > 1$) are essentially the same in all models (see Table 2).

(A color version of this figure is available in the online journal.)

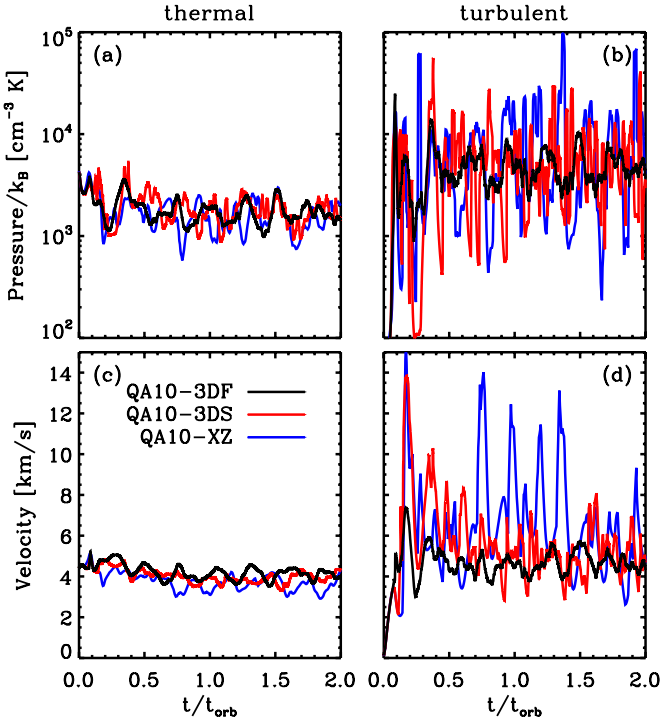

Figure 3. Time evolution of (a) thermal and (b) turbulent pressures at the midplane, together with the mass-weighted (c) thermal and (d) turbulent velocity dispersions of the diffuse component for models QA10-3DF (black), QA10-3DS (red), and QA10-XZ (blue). Boxcar averages with a window of $\Delta t = 0.02 t_{orb}$ are taken to reduce noisy spikes and show fluctuations clearly.

(A color version of this figure is available in the online journal.)

Kim et al. 2010).[8] At the midplane, thermal instability forms cold cloudlets, and subsequent gravitational accretion leads to growth of more massive clouds. The first star formation and SN feedback event is triggered at $t \sim 0.1 t_{orb} \sim 20$ Myr (see middle row of Figure 1), and many subsequent events follow. The feedback events disperse cold cloudlets and swell the gas disk vertically (see bottom row of Figure 1). Dispersed gas slows as it climbs vertically in the combined potential of stars and gas, and then falls back to the midplane. Gravitational condensation of clouds into larger structures leads to new high-density regions with subsequent star formation and feedback events. Driven by these processes, the gas disk undergoes a quasi-periodic cycle of vertical "breathing" oscillations with period of $t_{osc} \sim 0.5(\pi/G\rho_{sd})^{1/2}$ (see Figure 2), equal to ~60 Myr for model QA10. This is half of the free-particle vertical oscillation period because cloudlets collide at the midplane.

Figure 2 presents the time histories of (a) the disk scale height $H \equiv [\int \rho z^2 dV / \int \rho dV]^{1/2}$, (b) the SFR surface density Σ_{SFR}, and (c) the gaseous Toomre stability parameter $Q_g \equiv \kappa\sigma_x/\pi G\Sigma$, with $\sigma_x^2 \equiv \int (P + \rho v_x^2) dV / \int \rho dV$, for models QA10-3DF (black), QA10-3DS (red), and QA10-XZ (blue). All quantities reach quasi-steady saturated values after one orbit, implying that statistical measures can be computed starting at this epoch. All three models, with different azimuthal domains, are overall in very good agreement with each other, confirming the reliability of our previous XZ models and the 3DS models for the purposes of assessing mean values of H and Σ_{SFR}. The scale height, the SFR surface density, and the Toomre parameter have mean values $\langle H \rangle = 81$, 80, and 88 pc, $\langle \Sigma_{SFR} \rangle = 1.5$, 1.5, and $1.7 \times 10^{-3}\, M_\odot$ kpc^{-2} yr^{-1}, and $\langle Q_g \rangle = 1.7$, 1.8, and 1.8 for QA10-3DF, QA10-3DS, and QA10-XZ models, respectively. The angle brackets $\langle\rangle$ denote a time average over $t/t_{orb} = 1$–2 (note that in Paper I, time averages are taken for $t/t_{orb} = 2$–3). Since QA10-3DS and QA10-XZ models adopt $t_{bin} = 0.5 t_{orb} > t_{osc}$ for the purpose of computing Σ_{SFR} and heating rates, the temporal fluctuation in Σ_{SFR} is reduced for these models. Similarly, the spiky profiles shown in the QA10-3DS and QA10-XZ models are not seen in the QA10-3DF model due to the larger spatial averaging volume.

Figure 3 plots the time histories at the midplane of (a) thermal and (b) turbulent pressure in all QA10 models. As demonstrated in Paper I, the total pressure at the midplane, P_{tot}, is crucial because it must match the vertical weight of the ISM (i.e., dynamical equilibrium pressure), and because it is also directly related to Σ_{SFR} via feedback. Since P_{tot} consists of both thermal and turbulent components, which are independently connected to the SFR (see Section 3.3 and Paper I), it is useful to calculate the thermal and turbulent pressures separately by taking

[8] Although the specific initial conditions affect the initial model evolution, evolution at later stages and the resulting saturated-state statistical properties are similar irrespective of the choice of initial conditions.

Table 2
Disk Properties 1

Model (1)	$\log \Sigma_{\rm SFR}$ (2)	$\log P_{\rm th}/k_{\rm B}$ (3)	$\log P_{\rm turb}/k_{\rm B}$ (4)	n_0 (5)	$H_{\rm diff}$ (6)
QA02-3DF	-4.11 ± 0.32	2.23 ± 0.16	2.52 ± 0.35	0.19 ± 0.13	306 ± 111
QA02-3DS	-4.04 ± 0.09	2.29 ± 0.23	2.56 ± 0.54	0.14 ± 0.11	337 ± 100
QA02-XZ	-4.20 ± 0.23	1.94 ± 0.35	2.61 ± 1.51	0.05 ± 0.08	342 ± 111
QA05-3DF	-3.43 ± 0.27	2.70 ± 0.15	3.19 ± 0.35	0.53 ± 0.34	160 ± 53
QA05-3DS	-3.43 ± 0.06	2.69 ± 0.19	3.19 ± 0.38	0.35 ± 0.24	170 ± 29
QA05-XZ	-3.52 ± 0.12	2.53 ± 0.22	3.03 ± 0.72	0.39 ± 0.30	174 ± 37
QA10-3DF	-2.82 ± 0.12	3.23 ± 0.10	3.69 ± 0.15	1.46 ± 0.40	85 ± 13
QA10-3DS	-2.84 ± 0.03	3.25 ± 0.11	3.86 ± 0.42	1.47 ± 0.55	84 ± 12
QA10-XZ	-2.74 ± 0.11	3.24 ± 0.15	3.85 ± 0.60	1.12 ± 0.58	92 ± 18
QA20-3DF	-2.18 ± 0.06	3.79 ± 0.04	4.20 ± 0.09	3.43 ± 0.58	47 ± 4
QA20-3DS	-2.20 ± 0.02	3.86 ± 0.06	4.32 ± 0.23	3.83 ± 0.80	47 ± 5
QA20-XZ	-2.06 ± 0.10	3.86 ± 0.07	4.19 ± 0.63	2.76 ± 0.70	51 ± 5
R50-3DF	-3.02 ± 0.30	3.64 ± 0.19	3.60 ± 0.49	1.31 ± 0.88	99 ± 29
R50-3DS	-3.05 ± 0.05	3.72 ± 0.09	3.82 ± 0.53	1.34 ± 0.46	92 ± 13
R50-XZ	-2.96 ± 0.22	3.69 ± 0.16	3.31 ± 0.37	1.29 ± 0.58	97 ± 20

Notes. The temporal averages and standard deviations are taken over $t/t_{\rm orb} = 1$–2 for 3D models and $t/t_{\rm orb} = 2$–3 for XZ models. Column 2: logarithm of the SFR surface density ($M_\odot\,{\rm kpc}^{-2}\,{\rm yr}^{-1}$). Columns 3 and 4: logarithm of the midplane thermal and turbulent pressures over $k_{\rm B}$ (${\rm cm}^{-3}$ K). Column 5: midplane number density of hydrogen (${\rm cm}^{-3}$). Column 6: scale height of the diffuse component (pc). See Section 3.2 for definitions.

volume-weighted horizontal averages as

$$P_{\rm th} = \frac{\int_{z=-\Delta z/2}^{z=+\Delta z/2}\int\int P\Theta(n<n_{\rm GBC})dxdydz}{\int_{z=-\Delta z/2}^{z=+\Delta z/2}\int\int \Theta(n<n_{\rm GBC})dxdydz}, \quad (11)$$

$$P_{\rm turb} = \frac{\int_{z=-\Delta z/2}^{z=+\Delta z/2}\int\int \rho v_z^2\Theta(n<n_{\rm GBC})dxdydz}{\int_{z=-\Delta z/2}^{z=+\Delta z/2}\int\int \Theta(n<n_{\rm GBC})dxdydz}. \quad (12)$$

Here, to average only over diffuse gas, $\Theta(X)$ is 1 if the logical argument "X" is true and 0 otherwise. We choose $n_{\rm GBC} \equiv 50\,{\rm cm}^{-3}$ as the minimum density for GBCs that are compressed by self-gravity to higher thermal pressure than their surroundings.[9] In Figure 3, we have applied a boxcar average with window size of $\Delta t = 0.02 t_{\rm orb}$ to show time evolution clearly. The mean thermal and turbulent pressures at the midplane are quite similar among all QA10 models (see also Columns 3 and 4 of Table 2). Turbulent pressures in the QA10-3DS and QA10-XZ models fluctuate with larger amplitude than in the QA10-3DF model because of their smaller averaging domains.

Figures 3(c) and (d), respectively, show the mass-weighted thermal and turbulent vertical velocity dispersions of the diffuse component, given by

$$v_{\rm th,diff} \equiv \left(\frac{\int P\Theta(n<n_{\rm GBC})dxdydz}{\int \rho\Theta(n<n_{\rm GBC})dxdydz}\right)^{1/2},$$
$$v_{\rm z,diff} \equiv \left(\frac{\int \rho v_z^2\Theta(n<n_{\rm GBC})dxdydz}{\int \rho\Theta(n<n_{\rm GBC})dxdydz}\right)^{1/2}. \quad (13)$$

Since the mass-weighted velocity dispersions averaged over the whole simulation volume relate most closely to quantities that can be directly observed, we use these velocities as observational proxies in our simulations. The mass-weighted thermal velocity dispersions are $\sim 4\,{\rm km\,s}^{-1}$ for all QA10 models, while the turbulent velocity is higher in model QA10-XZ ($\langle v_{\rm z,diff}\rangle = 7.2 \pm 2.3\,{\rm km\,s}^{-1}$) than in models QA10-3DS ($\langle v_{\rm z,diff}\rangle = 5.1 \pm 1.0\,{\rm km\,s}^{-1}$) and QA10-3DF ($\langle v_{\rm z,diff}\rangle = 4.7 \pm 0.5\,{\rm km\,s}^{-1}$).

Since the midplane values of both thermal and turbulent pressures are in good agreement among all QA10 models, the differences of the mass-weighted turbulent velocity dispersions, which are averaged over the whole simulation domain, must arise from differences in the vertical profiles. To see this clearly, we define the mass-weighted, horizontally averaged velocity dispersions as functions of z:

$$v_{\rm th}(z) = \left[\frac{\int P\Theta(n<n_{\rm GBC})dxdy}{\int \rho\Theta(n<n_{\rm GBC})dxdy}\right]^{1/2},$$
$$v_z(z) = \left[\frac{\int \rho v_z^2\Theta(n<n_{\rm GBC})dxdy}{\int \rho\Theta(n<n_{\rm GBC})dxdy}\right]^{1/2}. \quad (14)$$

Figure 4 plots vertical profiles of (a) $\langle v_{\rm th}(z)\rangle$ and (b) $\langle v_z(z)\rangle$ based on time averages for the QA10-3DF (black), QA10-3DS (red), and QA10-XZ (blue) models. The vertical profiles of thermal velocity dispersion $\langle v_{\rm th}(z)\rangle$ show similar trends for all QA10 models, increasing as $|z|$ increases since the warm gas dominates at high-$|z|$. However, the vertical profiles of turbulent velocity dispersion $\langle v_z(z)\rangle$ in QA10-3D models are nearly flat or even decrease at high $|z|$, while $\langle v_z(z)\rangle$ in the QA10-XZ model secularly increases with $|z|$. This is presumably because the total mass swept up by an expanding shell is larger in 3D models (spherical volume $\propto r^3$) than in XZ models (cylindrical volume $\propto r^2 r_{\rm sh}$ for $L_y = 2r_{\rm sh}$). Although the feedback is normalized for the XZ models such that the injected momentum is the same as for 3D models (see Paper I), the resulting turbulent velocities at high $|z|$ are smaller in 3D because the larger swept-up mass in 3D reduces the mean velocity at large $|z|$. Near the midplane, at $|z| \lesssim H$ (i.e., where density is within a factor $\sim$3 of the

[9] We have checked that the exact choice of $n_{\rm GBC}$ does not significantly affect our statistical results for diffuse gas provided it is high enough to safely separate out high-pressure cold gas.

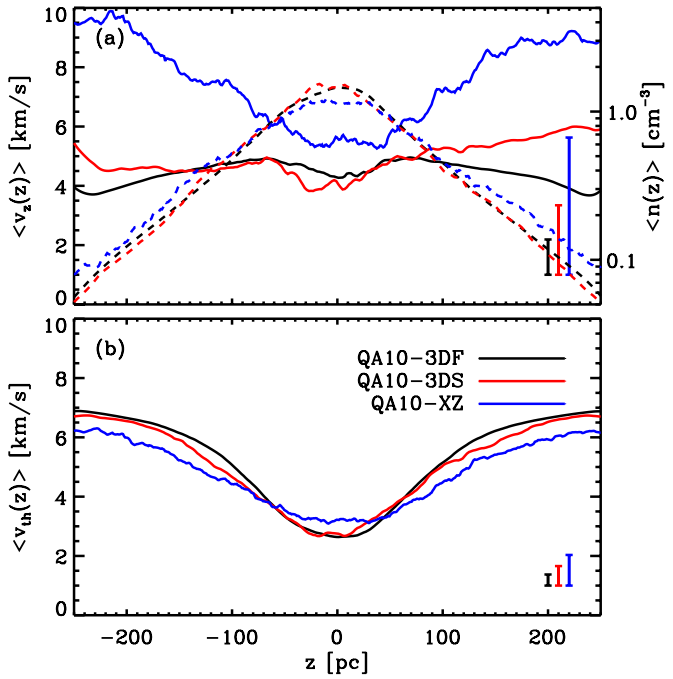

Figure 4. Temporally and horizontally averaged velocity dispersion profiles (solid curves) in z (see Equation (14)) for (a) vertical turbulent and (b) thermal components. The mean standard deviations of temporal fluctuations are indicated as errorbars in the bottom-right corner. In (a), the dashed curves and right axis show the corresponding density profiles.

(A color version of this figure is available in the online journal.)

midplane value; see right axis in Figure 4(a)), turbulent velocity dispersions for XZ models are similar to those for 3D models.

Figure 5 shows slices through the volume for a snapshot ($t/t_{\rm orb} = 1.12$) of model QA10-3DF after a quasi-steady state is reached. The structure of the ISM is filamentary, with high porosity and relatively large-scale structures due to the combined action of SN events and self-gravity. Some high-density cloudlets are located near SN shell boundaries, as shown in Paper I, although cloudlets are also present far from these shells. In Figure 6, we show (a) the column density of gas projected onto the horizontal plane and (b) the volume density averaged along the azimuthal (y) direction, for the same snapshot. Although Figure 6(a) contains a large-scale diagonal feature, examination of model animations over several orbits shows that this kind of sheared structure grows and then disperses before reaching very large amplitude. This is likely because continuous kinetic energy input from SN feedback keeps the turbulent velocity dispersion large enough to maintain Q_g within the range between 1.5 and 2 (see Figure 2(c)) in which swing amplification is not strong (e.g., Kim & Ostriker 2001, 2007; Kim et al. 2002).

Even without large-scale swing amplification, self-gravity (together with the gravity of the stellar disk) plays an important role in creating ISM structures. Based on inspection of the evolving structure in our models, cold cloudlets are seen to be drawn together by gravity to create more massive clouds. This process is possible only because the ISM is a two-phase cloud/intercloud medium. The thermal pressure of cold cloudlets approximately matches that of the surrounding warm medium at their surfaces, but the density in the cold medium is two orders of magnitude higher than the warm medium. As a consequence, cold cloudlets move freely through the warm medium, falling toward the midplane after reaching a maximum height. Self-gravity then aids their mutual collection to create a larger structure. The successive snapshots shown in Figure 7 illustrate the formation of a massive cloud by this process.

Statistical distributions of the density, pressure, and temperature provide a detailed picture of the thermodynamic state in our models. Figure 8 displays time-averaged probability distribution functions (PDFs) of the QA10-3DF model, based on time averages over $t/t_{\rm orb} = 1$–2. In Figure 8(a), the mass fraction of gas as a function of number density and thermal pressure is shown in logarithmic color scale. The majority of gas remains near the thermal equilibrium curve (solid line) defined by the time-averaged heating rate $\langle\Gamma\rangle = 0.61\Gamma_0$. Figures 8(b)–(d) plot (b) thermal pressure, (c) number density, and (d) temperature PDFs by mass (solid lines) and volume (dotted lines). The dashed lines in Figures 8(b) and (c) show the mean midplane thermal pressure $\langle P_{\rm th}/k_{\rm B}\rangle = 1.7\times10^3\,{\rm cm^{-3}\,K}$ and the mean midplane number density $\langle n_0\rangle = 2.0\,{\rm cm^{-3}}$ for the QA10-3DF model. The thermal pressure lies mainly between the minimum value for cold gas in equilibrium, $P_{\rm min}$, and the maximum value for warm gas in equilibrium, $P_{\rm max}$, with a peak at the mean midplane pressure. However, a significant amount of gas (∼30%–35% by mass) has pressure higher and lower than $P_{\rm max}$ and $P_{\rm min}$, respectively. The pressure distribution in our model is in part similar to that of driven turbulence simulations in thermally bistable flows (e.g., Gazol et al. 2005, 2009; Gazol & Kim 2013; Saury et al. 2013). Unlike those models, however, our models also contain high-pressure cold gas confined by self-gravity, and low-pressure warm gas found at high altitude. Shock-heated warm gas at high pressure is observed in both our models and in the non-self-gravitating, unstratified simulations of other groups.

The density and temperature PDFs show bimodal distributions with cold, dense and warm, rarefied phases as expected in the classical two-phase ISM (e.g., Field et al. 1969; Piontek & Ostriker 2004). However, unlike the classical picture, the distribution shows broadened peaks with a substantial fraction of gas out of equilibrium. These differences are due to several factors: strong turbulence that compresses and rarefies the gas continuously, SN events that produce thermal transitions (in part induced by expanding strong shocks), and a time-dependent heating rate such that the thermal equilibrium curve itself fluctuates. Since the level of turbulence in our models is transonic or slightly subsonic for warm gas, the unimodal PDFs expected in highly supersonic turbulent flows (Gazol et al. 2005) are not found here. Although velocity dispersions are ∼20% higher in the QA10-XZ model than in the 3D models, we find that the PDFs for all QA10 models are very similar since the differences in turbulence are small within one scale height ($|z| \lesssim 80\,{\rm pc}$) where the bulk of mass is found (see Figure 4).

In all our simulations, disk evolution at later times ($t > t_{\rm orb}$) is similar to that of the fiducial model. All models reach a quasi-steady state that includes strong turbulence, cyclic formation and destruction of GBCs, vigorous stirring of the population of small cloudlets, and quasi-periodic vertical disk oscillations. The vertical oscillations in our simulations are correlated over the whole simulation domain. This is likely because the initial collapse of non-turbulent, out-of-equilibrium gas to the midplane occurs simultaneously over the whole region.[10] Vertical oscillations would be present in reality, but they would be correlated only over a smaller horizontal domain,

[10] Real galactic disks span ∼10 kpc in radius, and any local vertical oscillations over scales of a few hundred pc would be difficult to discern. In addition, the presence of spiral arms, bars, minor mergers, etc. may limit the development of local oscillations driven by feedback from star formation.

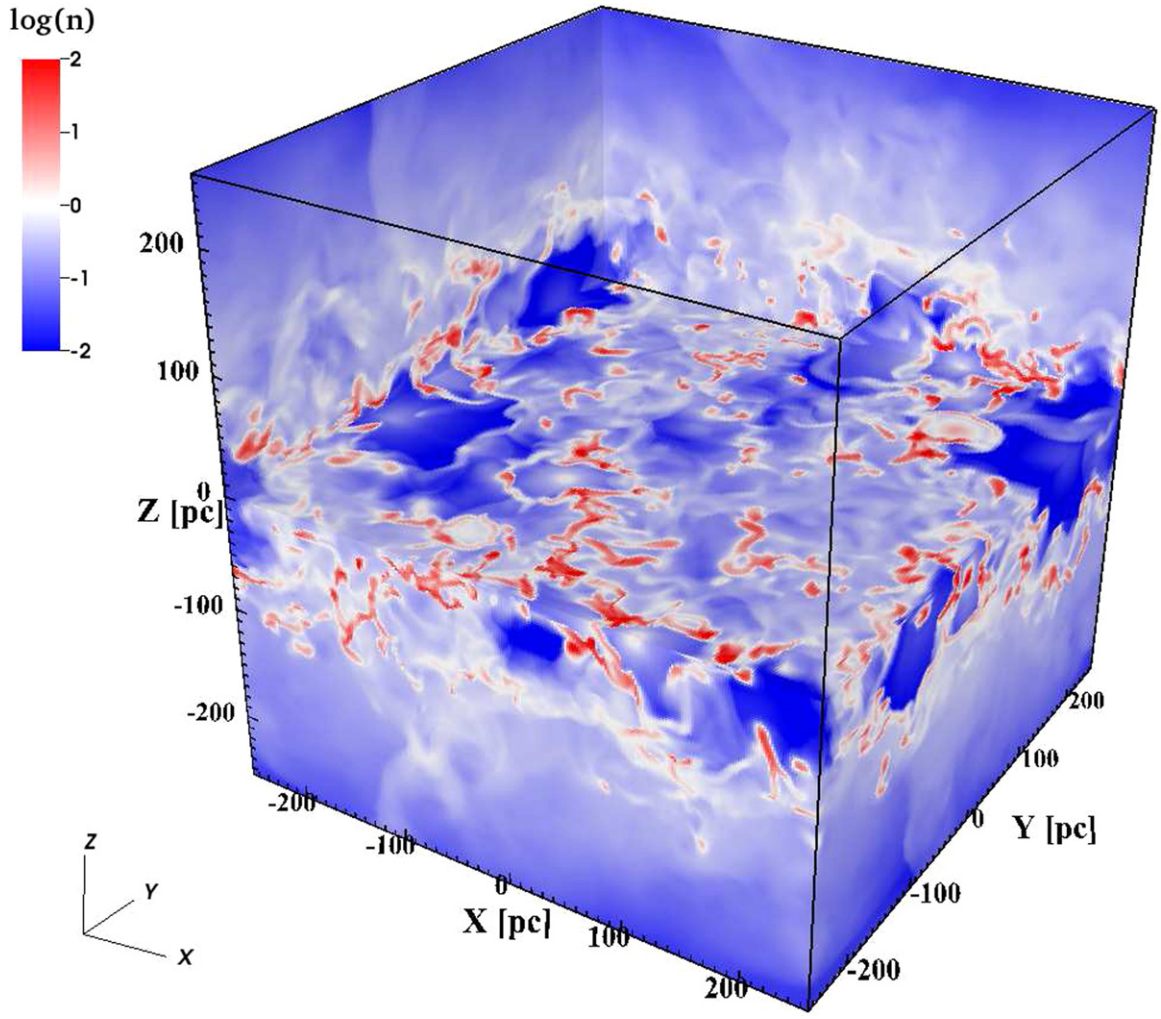

Figure 5. Density structure in solar-neighborhood model QA10-3DF at $t/t_{\rm orb} = 1.12$, after a fully turbulent state is reached. The colorbar labels $\log n$ (cm^{-3}) in five different planes ($x = \pm L_x/2$, $y = \pm L_y/2$, and $z = 0$). Cloudy/filamentary structure is evident, as well as dispersal of dense gas above and below the midplane by feedback-driven turbulence.

(A color version of this figure is available in the online journal.)

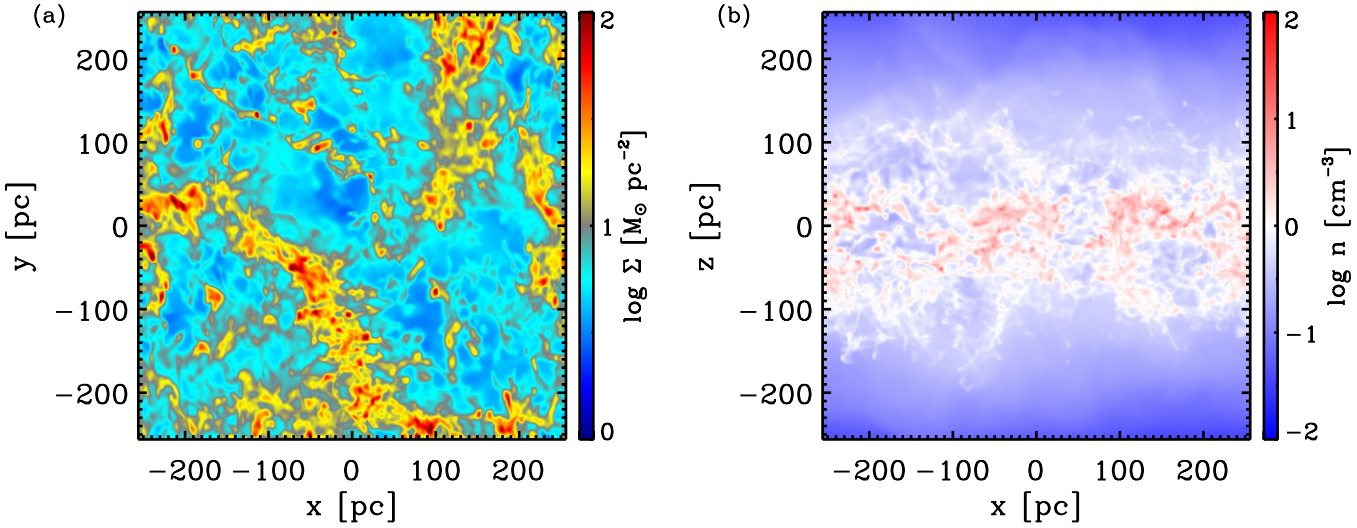

Figure 6. (a) Surface density projected on the horizontal plane for the same snapshot shown in Figure 5. The radial direction is along x, and the azimuthal direction is along y. The colorbar labels $\log \Sigma$ ($M_\odot$ pc^{-2}). (b) Radial-vertical density structure based on azimuthal (i.e., along y) average of the same snapshot shown in Figure 5. The colorbar labels $\log(n)$ (cm^{-3}).

(A color version of this figure is available in the online journal.)

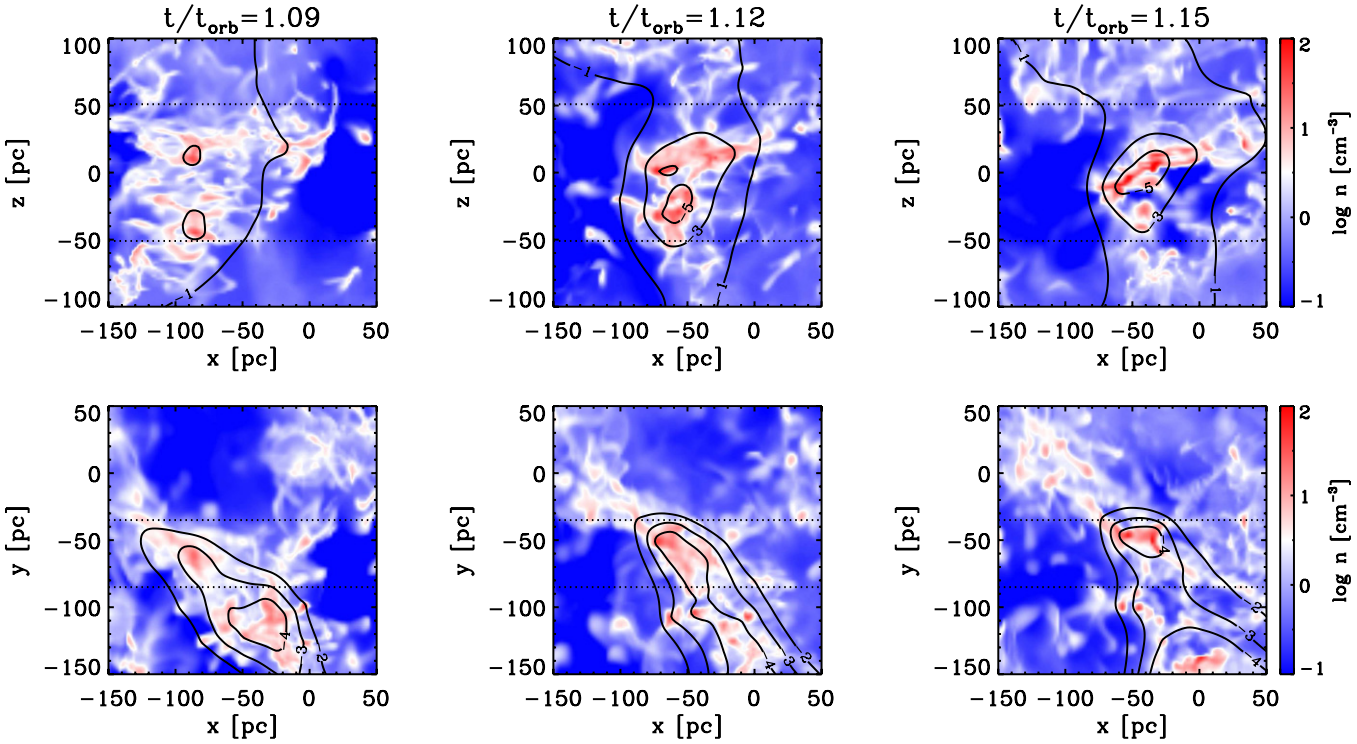

Figure 7. Example of cloud growth by gravitationally driven accretion. The top and bottom rows show snapshots on the radial-vertical and horizontal planes, respectively, of the number density averaged over the region $-85\,\mathrm{pc} \leqslant y \leqslant -35\,\mathrm{pc}$ (dotted lines in the bottom row) and $-50\,\mathrm{pc} \leqslant z \leqslant 50\,\mathrm{pc}$ (dotted lines in the top row) at $t/t_{\rm orb} = 1.09$ (left), 1.12 (center), and 1.15 (right). The mean perturbed gravitational potential $\Delta\Phi \equiv \Phi - \overline{\Phi}(z)$, where $\overline{\Phi}$ denotes the horizontally averaged potential, in units of $(\mathrm{km\ s^{-1}})^2$ is overlaid as contours. Cold cloudlets fall to the midplane, accrete surrounding gas, and merge together to grow into a massive cloud that dominates the gravitational potential.

(A color version of this figure is available in the online journal.)

comparable to the size that is affected by feedback from a given star-forming region. For all model series, $\Sigma_{\rm SFR}$ and $P_{\rm tot}$ increase as the gas surface density (Σ) and/or the depth of the gravitational potential well (depending on Σ and on the stellar density $\rho_{\rm sd}$) increase. The velocity dispersion $v_{\rm z,diff}$ is more or less constant independent of model parameters. Detailed scaling relations and statistical properties will be addressed below.

For models with low gas and stellar densities, the star formation events become rare and stochastic, leading to large amplitude fluctuations in $\Sigma_{\rm SFR}$. In high-$f_{\rm rad}$ models, the heating rate is highly sensitive to $\Sigma_{\rm SFR}$, again resulting in large temporal variation in ISM properties and $\Sigma_{\rm SFR}$. The XZ models in Paper I were unable to fully address the effect of strong temporal fluctuation of the SFR in low-$\Sigma_{\rm SFR}$ and high-$f_{\rm rad}$ models because it was necessary to adopt $t_{\rm bin}$ much longer than the realistic lifetime of massive stars (cf. Figure 2(b)). In the present 3DF models with large azimuthal domains, we can adopt $t_{\rm bin}$ close to the FUV luminosity-weighted life time $t_{\rm FUV} \sim 10$ Myr. Figure 9 plots the time evolution of $\Sigma_{\rm SFR}$ for all 3DF models. Relative to $t_{\rm orb}$, the fluctuation periods of $\Sigma_{\rm SFR}$ are similar for all the models shown since the ratio $t_{\rm osc}/t_{\rm orb} \approx 0.25\Omega/(4G\rho_{\rm sd})^{1/2} = 0.27$ is constant. The low-density and high-$f_{\rm rad}$ models show order-of-magnitude fluctuations in $\Sigma_{\rm SFR}$, while fluctuations are only at a factor of 2–3 level for models at higher density and $f_{\rm rad} = 1$. In the high-$f_{\rm rad}$ model, the large fluctuations of the SFR are self-reinforcing because fluctuations of the heating rate follow the SFR as $\Gamma \propto f_{\rm rad}\Sigma_{\rm SFR}$ and the resulting fluctuations in cold gas content lead to varying $\Sigma_{\rm SFR}$.

Figure 10 displays (a) the gas mass fraction in the density–pressure phase plane, and (b) thermal pressure, (c) number density, and (d) temperature PDFs of the R50-3DF enhanced-heating model with $f_{\rm rad} = 5.0$. While the ranges of pressure, density, and temperature are similar to the QA10 $f_{\rm rad} = 1$ model shown in Figure 8, this high-$f_{\rm rad}$ model shows higher mean thermal pressure, a lower fraction of cold, dense gas, and a broader peak in the pressure PDF. These differences are a consequence of both the higher heating rate and increased stochasticity of this model. For the R50-3DF model, the time evolution of the SFR in Figure 9 shows two distinct levels of $\Sigma_{\rm SFR}$ rather than the moderate fluctuations about a mean value seen for model QA10-3DF. Since the gas is approximately in instantaneous thermal equilibrium at either the high or low $\Sigma_{\rm SFR}$ state, with either a high or low heating rate and the corresponding equilibrium curve, traces of the two states are evident in the distributions shown in Figure 10(a). As a consequence of the well-separated high and low states, the time-averaged pressure PDF is quite broad. In spite of the two-state behavior of the R50-3DF model, the mean values of $\Sigma_{\rm SFR}$, Γ, $P_{\rm th}$, and n_0 are quite similar (see Table 2) to those in the R50-3DS and R50-XZ models, in which fluctuations are reduced by adopting $t_{\rm bin} = 0.5\,t_{\rm orb} > t_{\rm osc}$ for computing the heating rate.

Detailed examination of our low-density models (QA02-3DF and QA05-3DF) shows that stochasticity similarly leads to broadened distributions of $P_{\rm th}$ compared to the fiducial model. In real galaxies, regions with low gas and stellar densities also tend to have lower metallicity, such that $f_{\rm rad}$ increases, which could increase fluctuations even more compared to these models with $f_{\rm rad} = 1$. Even in highly stochastic 3DF models, however, we find that the mean saturated-state properties are similar to those found from XZ models, confirming the results of Paper I.

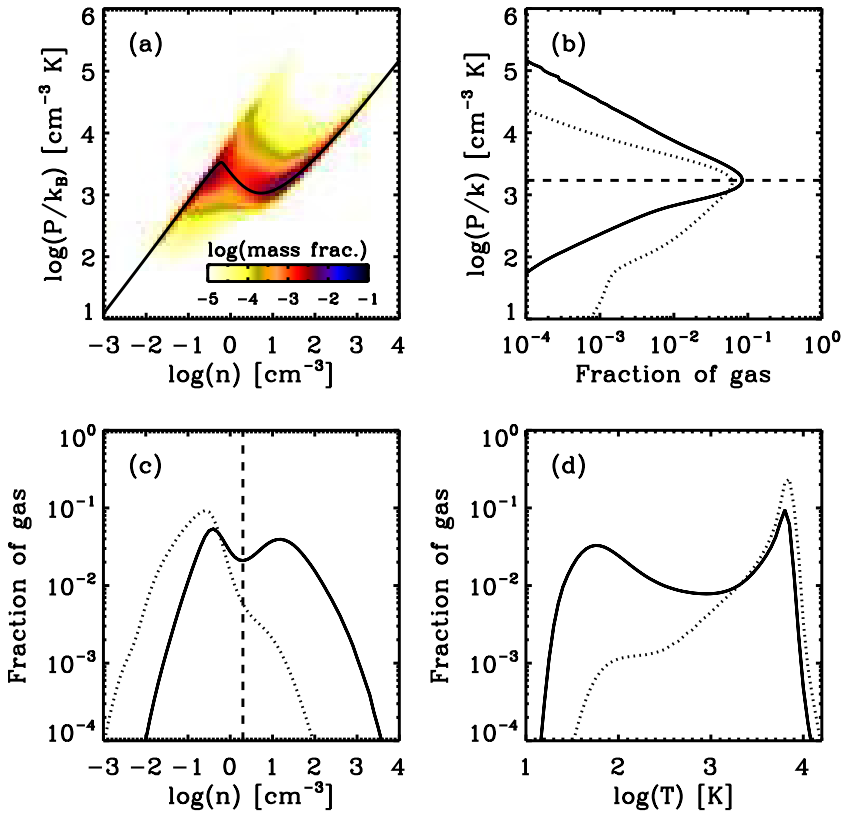

Figure 8. Probability density distributions of gas properties for the QA10-3DF model. Time averages are taken after saturation, over $t/t_{\rm orb} = 1$–2. (a) Logarithmic mass fractions of QA10-3DF model in the n–P plane. The solid curve indicates the locus of thermal equilibrium for the mean heating rate $\langle\Gamma\rangle = 0.61\Gamma_0$. (b)–(d) Mass-weighted (solid) and volume-weighted (dotted) PDFs for (b) thermal pressure, (c) number density, and (d) temperature. The dashed lines in (b) and (c) denote the mean midplane thermal pressure $\langle P_{\rm th}/k_{\rm B}\rangle = 1.7\times10^3\,{\rm cm^{-3}\,K}$ and number density $\langle n_0\rangle = 2.0\,{\rm cm^{-3}}$, respectively.

(A color version of this figure is available in the online journal.)

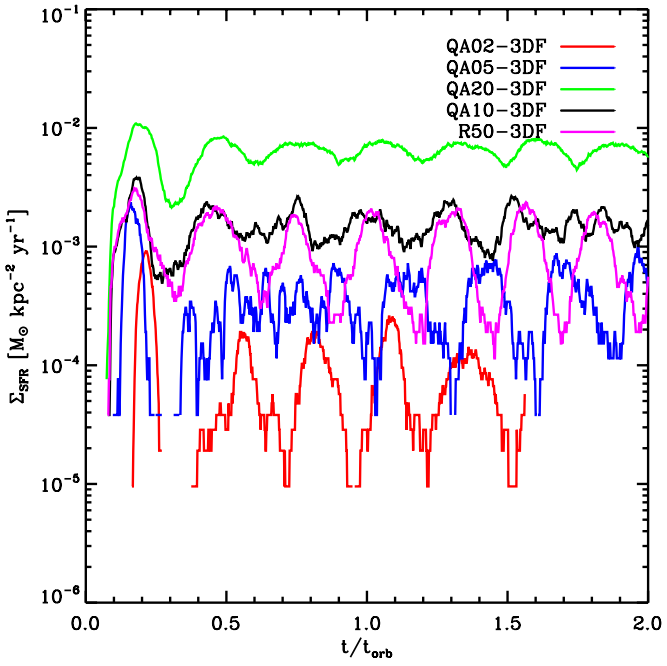

Figure 9. Time evolution of the SFR surface density $\Sigma_{\rm SFR}$ for all 3DF models. The amplitude of temporal fluctuations increases as $\Sigma_{\rm SFR}$ decreases, because the system is more stochastic.

(A color version of this figure is available in the online journal.)

3.2. Statistical Properties

All our models reach a quasi-steady state after two or three vertical oscillation times (see Figure 9), which is $<t_{\rm orb}$ for our model parameters. We thus investigate statistical properties of 3D models by averaging over $t/t_{\rm orb} = 1$–2. Tables 2 and 3 list the mean values and standard deviations of key physical quantities used in Paper I to test the thermal/dynamical equilibrium model of OML10 and OS11. In the tables, we present the results for all 3DF models together with the corresponding 3DS and XZ counterparts. In Figures 11–17, we also include results from additional 3DS models without 3DF counterparts. Hereafter, in reporting properties of the models, we use time averages over $t/t_{\rm orb} = 1$–2 for 3D models and $t/t_{\rm orb} = 2$–3 for XZ models (as in Paper I), unless stated otherwise. Angle brackets will be omitted for convenience.

Column 1 of Tables 2 and 3 gives the name of each model, consisting of the model name listed in Table 1 together with suffixes of 3DF, 3DS, and XZ to indicate the simulation domain size and geometry. In Table 2, Column 2 lists $\log\Sigma_{\rm SFR}$ in units of $M_\odot\,{\rm kpc^{-2}\,yr^{-1}}$. We list in Columns 3 and 4 $\log(P_{\rm th}/k_{\rm B})$ and $\log(P_{\rm turb}/k_{\rm B})$, respectively, in units of ${\rm cm^{-3}\,K}$. Column 5 gives the midplane hydrogen number density n_0 of the diffuse component in units of ${\rm cm^{-3}}$, defined in the same way with Equation (11) but for number density n rather than thermal pressure P in the integrand. Similarly, the scale height of the diffuse gas $H_{\rm diff} \equiv [\int \rho z^2\Theta(n < n_{\rm GBC})dV/\int\rho\Theta(n < n_{\rm GBC})dV]^{1/2}$ is listed in Column 6 in units of pc.

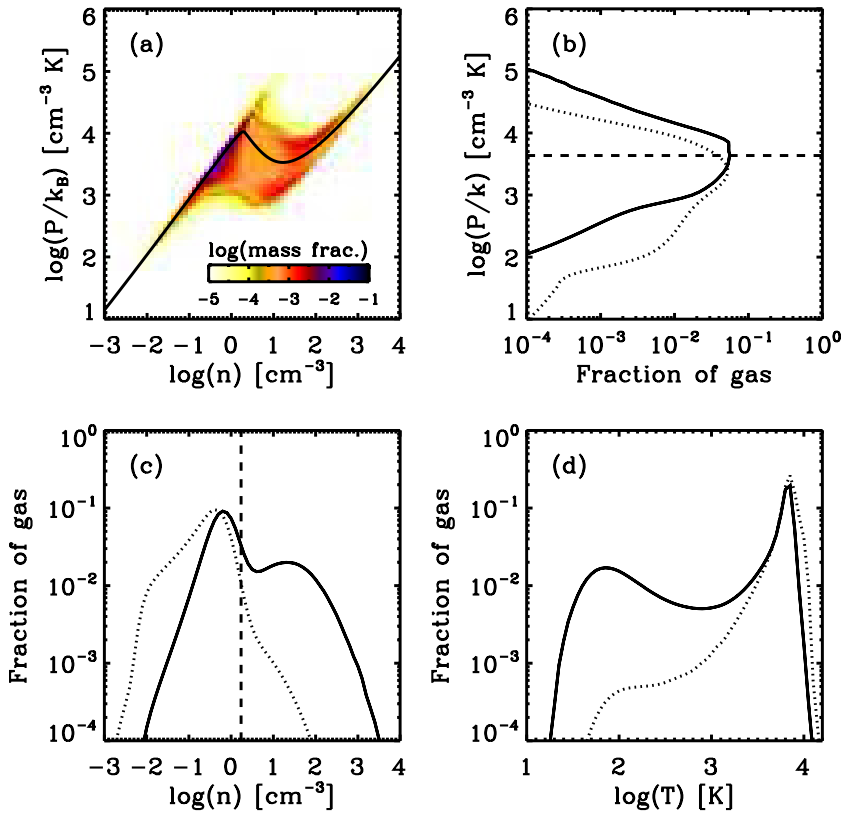

Figure 10. Same as Figure 8, but for model R50-3DF with high radiation feedback efficiency $f_{\rm rad} = 5.0$. Comparing panel (a) to Figure 8(a), signatures of a "high" and a "low" state are evident in this time-averaged distribution. For these states, the thermal equilibrium curve lies either above ("high" state) or below ("low" state) the thermal equilibrium curve at the mean heating rate of $\langle\Gamma\rangle = 1.9\Gamma_0$ (heavy curve in panel (a)). The mean midplane thermal pressure is $\langle P_{\rm th}/k_{\rm B}\rangle = 4.3 \times 10^3\,{\rm cm^{-3}\,K}$, and the mean midplane number density is $\langle n_0\rangle = 1.7\,{\rm cm^{-3}}$, as indicated in panels (b) and (c).

(A color version of this figure is available in the online journal.)

Table 3
Disk Properties 2

Model (1)	$v_{\rm z,diff}$ (2)	$v_{\rm th,diff}$ (3)	α_v (4)	α_P (5)	$f_{\rm diff}$ (6)	$\tilde{f}_w$ (7)
QA02-3DF	4.33 ± 1.07	4.07 ± 0.57	2.13 ± 0.64	2.95 ± 1.70	0.99 ± 0.01	0.21 ± 0.17
QA02-3DS	4.73 ± 1.75	4.22 ± 0.62	2.26 ± 1.00	2.86 ± 2.49	0.99 ± 0.02	0.34 ± 0.14
QA02-XZ	6.20 ± 4.57	3.27 ± 0.78	4.59 ± 5.56	5.75 ± 16.94	0.92 ± 0.07	0.23 ± 0.12
QA05-3DF	5.03 ± 1.00	3.85 ± 0.78	2.71 ± 0.97	4.09 ± 2.73	0.95 ± 0.03	0.26 ± 0.16
QA05-3DS	5.11 ± 1.43	3.90 ± 0.26	2.72 ± 0.99	4.09 ± 3.02	0.96 ± 0.03	0.30 ± 0.05
QA05-XZ	6.28 ± 2.95	3.25 ± 0.43	4.74 ± 3.65	4.16 ± 5.46	0.90 ± 0.06	0.25 ± 0.07
QA10-3DF	4.67 ± 0.47	4.11 ± 0.26	2.29 ± 0.31	3.88 ± 1.21	0.88 ± 0.03	0.34 ± 0.06
QA10-3DS	5.11 ± 1.01	3.88 ± 0.23	2.73 ± 0.71	5.08 ± 4.06	0.87 ± 0.05	0.32 ± 0.05
QA10-XZ	7.23 ± 2.28	3.73 ± 0.42	4.75 ± 2.51	5.02 ± 5.73	0.77 ± 0.09	0.32 ± 0.07
QA20-3DF	5.05 ± 0.32	4.47 ± 0.22	2.27 ± 0.20	3.53 ± 0.58	0.72 ± 0.03	0.41 ± 0.05
QA20-3DS	5.71 ± 0.68	4.35 ± 0.18	2.72 ± 0.43	3.86 ± 1.55	0.71 ± 0.04	0.38 ± 0.04
QA20-XZ	6.94 ± 1.67	4.59 ± 0.22	3.29 ± 1.12	3.17 ± 3.16	0.54 ± 0.06	0.46 ± 0.05
R50-3DF	5.51 ± 1.18	5.35 ± 0.93	2.06 ± 0.59	1.92 ± 1.12	0.91 ± 0.07	0.61 ± 0.26
R50-3DS	4.48 ± 1.18	5.77 ± 0.21	1.60 ± 0.32	2.25 ± 1.54	0.91 ± 0.03	0.74 ± 0.06
R50-XZ	4.49 ± 1.85	5.70 ± 0.49	1.62 ± 0.52	1.42 ± 0.39	0.85 ± 0.07	0.73 ± 0.12

Notes. The temporal averages and standard deviations are taken over $t/t_{\rm orb} = 1$–2 for 3D models and $t/t_{\rm orb} = 2$–3 for XZ models. Columns 2 and 3: vertical turbulent and thermal velocity dispersions of the diffuse gas (km s^{-1}). Columns 4 and 5: ratios of total pressure to thermal pressure calculated from the mass-weighted velocity dispersions (α_v) and the midplane pressures (α_P). Columns 6 and 7: mass fraction of the diffuse gas ($f_{\rm diff}$), and the square of mass-weighted thermal to warm-medium thermal speed ($v^2_{\rm th,diff}/c^2_w = \tilde{f}_w$) in the diffuse gas. See Section 3.2 for definitions.

In Table 3, Columns 2 and 3 list, respectively, $v_{\rm z,diff}$ and $v_{\rm th,diff}$ in units of km s^{-1}. In Columns 4 and 5, we list, respectively, the ratios of total-to-thermal pressure defined in two different ways, $\alpha_v \equiv (v^2_{\rm th,diff} + v^2_{\rm z,diff})/v^2_{\rm th,diff}$ and $\alpha_P \equiv (P_{\rm th} + P_{\rm turb})/P_{\rm th}$. Here, α_v averages over the whole volume, while α_P averages only at the midplane. Column 6 gives $f_{\rm diff}$, the mass fraction of the diffuse component ($n < n_{\rm GBC}$), and Column 7 gives $\tilde{f}_w \equiv v^2_{\rm th,diff}/c^2_w$, the ratio of the mass-weighted sound speed

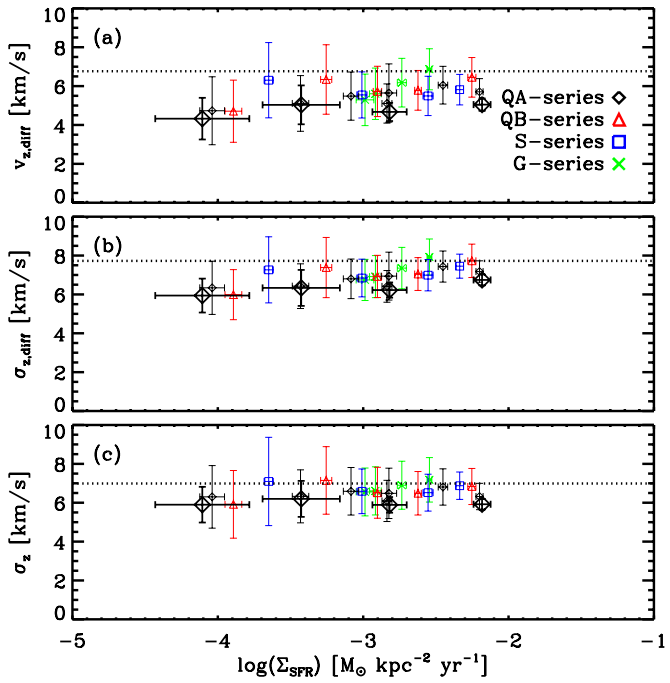

Figure 11. (a) Vertical turbulent velocity dispersion of the diffuse gas $v_{z,\rm diff}$, (b) total (turbulent+thermal) velocity dispersion of the diffuse gas $\sigma_{z,\rm diff}$, and (c) total velocity dispersion of all the gas (diffuse + GBC) σ_z, as functions of the SFR surface density $\Sigma_{\rm SFR}$. Results for all 3D models except the R series are shown; the thick large symbols denote the results from 3DF models, while the thin small symbols denote the results from 3DS models. The points and errorbars give the mean values and standard deviations over $t/t_{\rm orb} = 1$–2. Mean values from the 3D models are $v_{z,\rm diff} = 5.6 \pm 0.6\,{\rm km\,s^{-1}}$, $\sigma_{z,\rm diff} = 6.9 \pm 0.5\,{\rm km\,s^{-1}}$, and $\sigma_z = 6.5 \pm 0.4\,{\rm km\,s^{-1}}$. The horizontal dotted lines indicate the mean values ($v_{z,\rm diff} = 6.8 \pm 0.6\,{\rm km\,s^{-1}}$, $\sigma_{z,\rm diff} = 7.7 \pm 0.6\,{\rm km\,s^{-1}}$, and $\sigma_z = 7.0 \pm 0.4\,{\rm km\,s^{-1}}$) from all XZ models (Paper I) except the R series. Due to geometric effects, velocity dispersions from the XZ models are slightly larger than those from the 3D models.

(A color version of this figure is available in the online journal.)

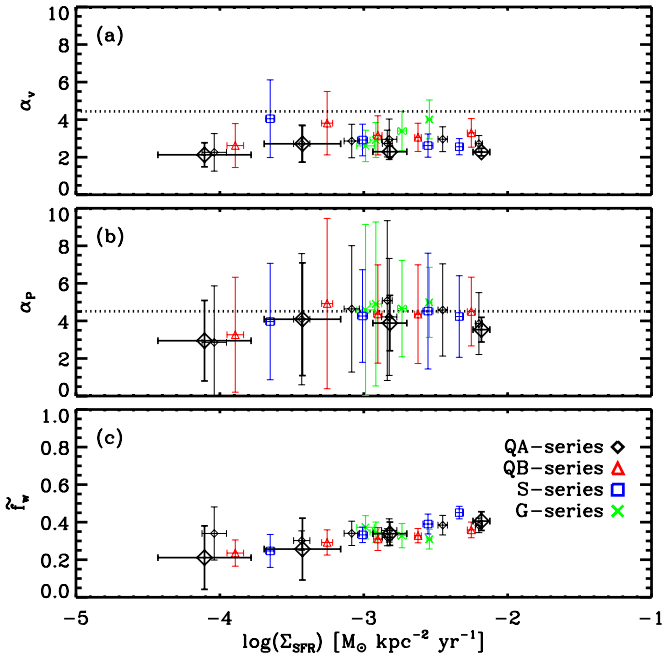

Figure 12. (a) Ratio of total-to-thermal velocity dispersion for the diffuse gas $\alpha_v \equiv 1 + v^2_{z,\rm diff}/v^2_{\rm th,diff}$ for the velocity dispersion weighted by mass over the whole domain; (b) ratio of total-to-thermal pressure for gas at the midplane $\alpha_P \equiv 1 + P_{\rm turb}/P_{\rm th}$, and (c) ratio of mass-weighted thermal-to-warm-medium thermal speed $v^2_{\rm th,diff}/c^2_w = \tilde{f}_w$. Results for all 3D models except the R series are shown. Symbols have the same meanings as in Figure 11. The dotted lines in (a) and (b) are the mean values of all XZ models (Paper I), $\alpha_v = 4.4$ and $\alpha_P = 4.5$. For 3D models, α_P is consistent with the value in XZ models, but α_v is smaller (see text). The quantity $\tilde{f}_w$ (essentially the warm mass fraction) ranges over 0.2–0.5 as in Paper I.

(A color version of this figure is available in the online journal.)

to the thermal velocity of warm gas (this is essentially equal to the warm gas fraction of mass in the diffuse component); these parameters are used in the OML10 theory.

Figure 11 plots the mean values of (a) $v_{z,\rm diff}$, (b) $\sigma_{z,\rm diff} \equiv (v^2_{z,\rm diff} + v^2_{\rm th,diff})^{1/2}$, and (c) the velocity dispersion of whole medium $\sigma_z \sim f^{1/2}_{\rm diff}\sigma_{z,\rm diff}$, as functions of $\Sigma_{\rm SFR}$ for all 3D models except the R series. The dotted horizontal line in each panel denotes the mean value from all XZ models (the models of Paper I). The mean values of all 3D models give $v_{z,\rm diff} = 5.6 \pm 0.6\,{\rm km\,s^{-1}}$, $\sigma_{z,\rm diff} = 6.9 \pm 0.5\,{\rm km\,s^{-1}}$, and $\sigma_z = 6.5 \pm 0.4\,{\rm km\,s^{-1}}$. As in Paper I, we find that the velocity dispersion is more or less constant over two orders of magnitude in $\Sigma_{\rm SFR}$. Due to geometrical effects in the expansion of SN remnants (see Section 3.1), turbulent velocity dispersions are slightly smaller (about 18%) in 3D models than in XZ models.

Figure 12 plots the mean values of (a) α_v, (b) α_P, and (c) $\tilde{f}_w$ as functions of $\Sigma_{\rm SFR}$ for all 3D models except the R series. The quantities α_v and α_P indicate whether the velocity dispersion and pressure in the ISM is thermally ($\alpha < 2$) or dynamically ($\alpha > 2$) dominated. The dotted lines in (a) and (b) indicate the mean values of $\alpha_v = 4.4$ and $\alpha_P = 4.5$ found from XZ models in Paper I. In XZ models, $\alpha_v \sim \alpha_P$ even though both $v_{\rm th}(z)$ and $v_z(z)$ vary significantly along the vertical direction since the profiles have similar shape (see blue lines in Figure 4). In contrast, the vertical profiles of thermal and turbulent velocity dispersions have different shapes in 3D models (see black and red lines in Figure 4). This results in differences between α_v and α_P. Averaging over all models except the R series yields $\alpha_v = 2.9$ and $\alpha_P = 4.2$, showing that the turbulent component of the mass-weighted velocity dispersion underestimates the midplane value. In the remaining sections, we will use α_P as a representative value, rather than α_v. Figure 12(c) shows that the warm mass fraction $\tilde{f}_w$ remains in the range 0.2–0.5 for all models, as previously found in Paper I. The fiducial value $\tilde{f}_w \sim 0.5$ adopted in OML10 is consistent with the range of our simulations.

3.3. Comparison with Thermal/Dynamical Equilibrium Model

It is natural to expect that a disk system that reaches a quasi-steady state satisfies vertical dynamical equilibrium in an average sense. That is, the diffuse ISM must maintain force balance between upward pressure forces (thermal and turbulent) and downward gravitational forces (arising from the diffuse gas itself as well as stars, dark matter, and GBCs; Piontek & Ostriker 2007; Koyama & Ostriker 2009b; OML10; Paper I). By taking time and horizontal averages, the vertical momentum equation in equilibrium can be written (OML10; Paper I) as $P_{\rm tot} = P_{\rm tot,DE}$ for

$$P_{\rm tot,DE} \equiv f_{\rm diff}\frac{\pi G\Sigma^2}{4}\left\{(2-f_{\rm diff}) + \left[(2-f_{\rm diff})^2 + \frac{32\sigma^2_{z,\rm diff}\rho_{\rm sd}}{\pi^2 G\Sigma^2}\right]^{1/2}\right\}, \quad (15)$$

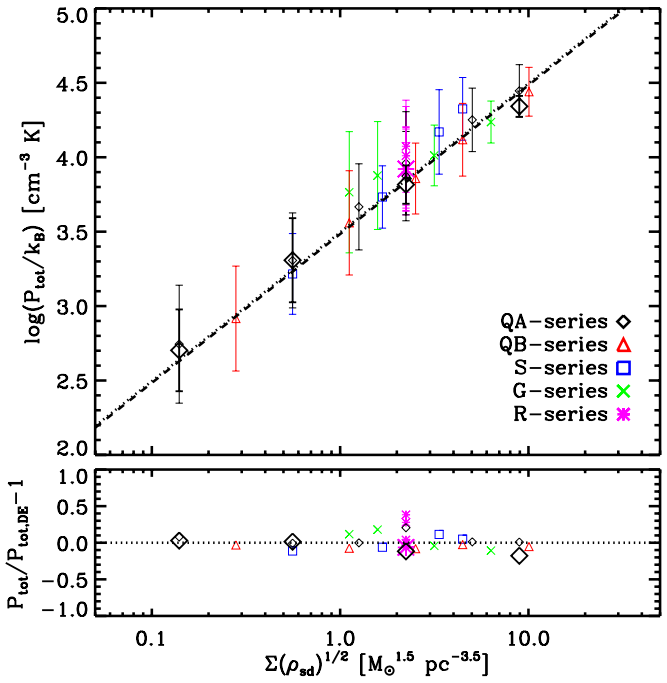

Figure 13. Top: total pressure of the diffuse gas measured in the simulations as a function of $\Sigma\sqrt{\rho_{\rm sd}}$. The symbols denote the same meanings as in Figure 11. The dashed and dotted lines show our best fit for all 3D models and XZ models, respectively. The good agreement between the two confirms the reliability of XZ models from Paper I. Bottom: relative differences between the measured midplane pressure $P_{\rm tot}$ and the pressure predicted for dynamical equilibrium $P_{\rm tot,DE}$ using Equation (15). The mean relative difference is only 12%, showing that vertical dynamical equilibrium indeed holds in an average sense.

(A color version of this figure is available in the online journal.)

where $P_{\rm tot,DE}$ represents the weight of the diffuse ISM.[11] Note that in OML10, $c_w^2 \tilde{f}_w \alpha$ was used instead of $\sigma_{\rm z,diff}^2$, but here we use the latter, as the total vertical velocity dispersion $\sigma_{\rm z,diff}$ is directly measurable in our simulations. Since in Section 3.2 we explicitly measure $f_{\rm diff}$ and $\sigma_{\rm z,diff}$ as well as $P_{\rm tot}$ for given input parameters (Σ, $\rho_{\rm sd}$), a direct comparison between $P_{\rm tot,DE}$ and $P_{\rm tot}$ is possible.

Figure 13 gives *measured* total pressure $P_{\rm tot}$ as a function of $\Sigma\sqrt{\rho_{\rm sd}}$ for all 3D models. The relative difference between *measured* and *predicted* (dynamical equilibrium) total pressure, $P_{\rm tot}/P_{\rm tot,DE} - 1$, is shown in the bottom panel. The mean relative difference is only 12%, showing that vertical dynamical equilibrium indeed holds. For the models we consider here, in which the external gravity exceeds the self-gravity of the diffuse gas, the last term in the square root of Equation (15) is dominant, and we expect

$$P_{\rm tot,DE} \approx f_{\rm diff}\sigma_{\rm z,diff}\Sigma(2G\rho_{\rm sd})^{1/2}. \quad (16)$$

If $f_{\rm diff}\sigma_{\rm z,diff}$ is insensitive to model parameters (as in Paper I) and $P_{\rm tot} \approx P_{\rm tot,DE}$, then the midplane total pressure is expected to correlate with $\Sigma\sqrt{\rho_{\rm sd}}$. This correlation is evident in the dashed line in Figure 13; the best fit coefficient for the 3D model results yields:

$$P_{\rm tot} = 9.6\times10^3 k_{\rm B}\ {\rm cm^{-3}\ K}\left(\frac{\Sigma}{10\,M_\odot\,{\rm pc^{-2}}}\right)\left(\frac{\rho_{\rm sd}}{0.1\,M_\odot\,{\rm pc^{-3}}}\right)^{1/2}. \quad (17)$$

In Figure 13, we overplot as a dotted line the best fit for the XZ models (Equation (37) in Paper I), which agrees very well with the dashed line and the 3D model results.

In addition to the force balance between total pressure and gravity, individual balances between thermal cooling and heating, and between turbulence driving and dissipation, are expected for a quasi-steady state. The gas is heated by FUV radiation from newly formed massive stars, with a heating rate that varies in proportion to the SFR (see Equation (10)). Owing to the very short cooling time compared to the dynamical time, the gas generally resides near thermal equilibrium, although a non-negligible fraction deviates from thermal equilibrium due to strong turbulence and temporal heating fluctuations (see Figures 8 and 10). Near the midplane, where GBCs and stars form, a cold phase should coexist with the warm phase, such that the midplane thermal pressure $P_{\rm th}$ should lie between $P_{\rm min}$ and $P_{\rm max}$. Figures 8 and 10 indeed show that the pressure lies in the neighborhood defined by $P_{\rm min}$ and $P_{\rm max}$ for the mean heating rate.

In OML10, the mean value of $P_{\rm th}$ at the midplane is assumed to approach the geometric-mean pressure $P_{\rm two} \equiv (P_{\rm min}P_{\rm max})^{1/2}$. The adopted cooling function and heating rate given by Equations (6) and (10) yield $P_{\rm two}/k_{\rm B} = 3.1\times10^3\,{\rm cm^{-3}\,K}(f_{\rm rad}\Sigma_{\rm SFR}/\Sigma_{\rm SFR,0})$, assuming that the contribution from the metagalactic FUV radiation is negligible. Our measurements for the mean value of $\Sigma_{\rm SFR}$ from the numerical simulations give the mean values of $P_{\rm two}$ for each model, which can be directly compared to the values of the measured mean midplane thermal pressure $P_{\rm th}$. Figure 14 plots $P_{\rm th}/P_{\rm two}$ as a function of $\Sigma_{\rm SFR}$ for all 3D models. The errorbars denote the standard deviations of temporal fluctuation, which amount to ~0.2–0.3 dex. Our best fit for 3D results,

$$\frac{P_{\rm th}}{P_{\rm two}} = 1.09\left(\frac{\Sigma_{\rm SFR}}{10^{-3}\,M_\odot\,{\rm kpc^{-2}\,yr^{-1}}}\right)^{-0.14}, \quad (18)$$

is shown as the dashed line, while the dotted line denotes the best fit for XZ models from Paper I. We conclude that $P_{\rm th}$ is indeed comparable to $P_{\rm two}$, over two orders of magnitude variation in $\Sigma_{\rm SFR}$. Our results show that $P_{\rm th} \sim P_{\rm two}$ within 60%, supporting the approximation adopted in the analytic theory of OML10. The mean values of the midplane thermal pressure in 3D models are slightly higher (~20%) than that of the XZ models, but the difference is smaller than the temporal fluctuations. Significant warm gas in the R50-3DF model (big magenta asterisk) puts it at lower average pressure than the mean relation; as discussed in Section 3.1, there are also large fluctuations in this model.

Dynamical energy injection through SN feedback connects the turbulent pressure and the SFR, similar to the connection between thermal pressure and the SFR from UV heating. Since the turbulent velocity dispersion does not evolve secularly (see Figure 3), the rate of turbulence driving must balance turbulent dissipation. The rate of turbulent driving per unit area per unit mass is expected to be $\propto (p_*/m_*)\Sigma_{\rm SFR}$, where p_* is the mean radial momentum injected to the ISM by an expanding SN remnant, and m_* is the total mass in stars per SN (averaged over the stellar mass function). For spherical blasts centered on the midplane, the vertical momentum injection rate per unit area

[11] In observational estimates, it is often assumed that all of the gas is in vertical equilibrium. Equation (15) instead represents the case in which all of the gas contributes to the vertical gravity, but only the diffuse gas (a fraction $f_{\rm diff}$ of the total) is in vertical equilibrium. For outer disks (as studied here) most gas is diffuse ($f_{\rm diff} \sim 1$), but for inner disks an increasing fraction of the mass may be in GBCs that are at higher pressure than their surroundings.

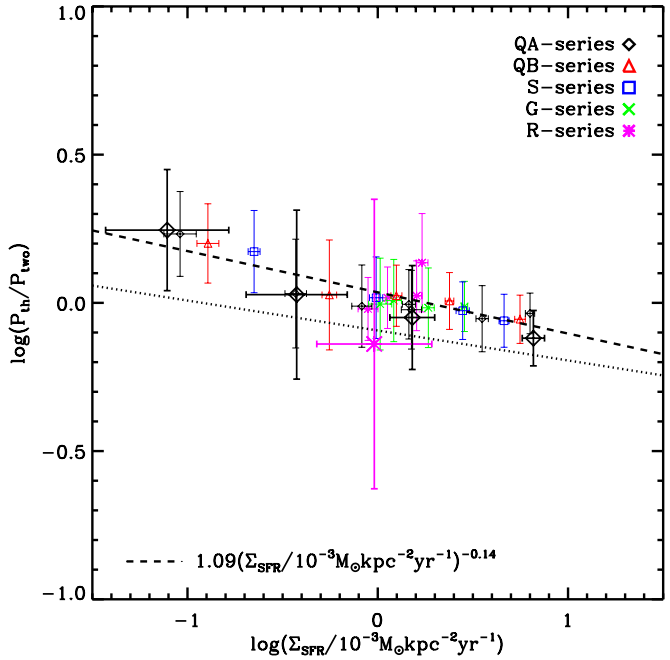

Figure 14. Measured midplane thermal pressure of the diffuse gas $P_{\rm th}$ relative to the two-phase thermal equilibrium pressure $P_{\rm two}$ as a function of $\Sigma_{\rm SFR}$. The symbols have the same meanings as in Figure 11. The dashed and dotted lines give the best fits for 3D and XZ models, respectively. The result from our simulations that $P_{\rm th} \sim P_{\rm two} \propto \Sigma_{\rm SFR}$ over more than two orders of magnitude in $\Sigma_{\rm SFR}$ implies that the radiative heating from star formation is balanced by cooling within a local (vertical) dynamical time.

(A color version of this figure is available in the online journal.)

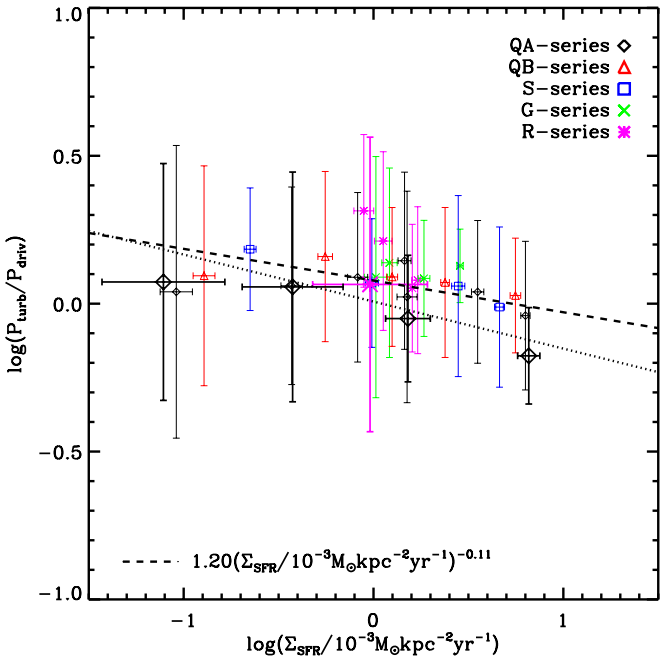

Figure 15. Measured midplane turbulent pressure of the diffuse gas $P_{\rm turb}$ relative to the characteristic vertical momentum flux injected by star formation feedback $P_{\rm driv}$ (see text), as a function of $\Sigma_{\rm SFR}$. The symbols have the same meanings as in Figure 11. The dashed and dotted lines give the best fits for 3D and XZ models, respectively. The result that $P_{\rm turb} \sim P_{\rm driv} \propto \Sigma_{\rm SFR}$ from our simulations, over more than two orders of magnitude in $\Sigma_{\rm SFR}$, implies that the turbulent energy driving from star formation is balanced by dissipation within a local (vertical) dynamical time.

(A color version of this figure is available in the online journal.)

to each side of the disk is $P_{\rm driv} = 0.25(p_*/m_*)\Sigma_{\rm SFR}$ (Paper I, OS11, SO12). The turbulent momentum flux in the vertical direction through the disk can be expressed as $P_{\rm turb} \equiv f_p P_{\rm driv}$, where $f_p \sim 1$ if dissipation balances driving within a dynamical time scale.

Using the adopted value $p_*/m_* = 3000\,{\rm km\,s^{-1}}$, the fiducial momentum injection rate varies with the SFR as $P_{\rm driv}/k_{\rm B} = 3.6\times10^3\,{\rm cm^{-3}\,K}(\Sigma_{\rm SFR}/10^{-3}\,M_\odot\,{\rm kpc^{-2}\,yr^{-1}})$. We make a direct comparison between the measured midplane turbulent pressure $P_{\rm turb}$ and $P_{\rm driv}$. Figure 15 plots the mean values of $f_p \equiv P_{\rm turb}/P_{\rm driv}$ as a function of $\Sigma_{\rm SFR}$ for all 3D models. The errorbars denote the standard deviations of temporal fluctuations, which amount to ∼0.3–0.6 dex. The dashed line is our best fit omitting the R series,

$$\frac{P_{\rm turb}}{P_{\rm driv}} = 1.20\left(\frac{\Sigma_{\rm SFR}}{10^{-3}\,M_\odot\,{\rm kpc^{-2}\,yr^{-1}}}\right)^{-0.11}, \qquad (19)$$

while the fit for the XZ models (Paper I) is overplotted as a dotted line with slightly steeper slope of −0.17. The results from the 3D models are in overall good agreement with our previous XZ models of Paper I, confirming that f_p is order-unity and approximately constant for a wide range of disk conditions and SFRs (see also SO12, which shows that f_p is similar in the starburst regime).

Since $P_{\rm th} \sim P_{\rm two}$ and $P_{\rm turb} \sim P_{\rm driv}$, both thermal and turbulent pressures at the midplane are nearly linearly proportional to $\Sigma_{\rm SFR}$. Following Paper I, we define

$$\frac{P_{\rm th}/k_B}{10^3\,{\rm cm^{-3}\,K}} \equiv \eta_{\rm th}\frac{\Sigma_{\rm SFR}}{10^{-3}\,M_\odot\,{\rm kpc^{-2}\,yr^{-1}}}, \qquad (20)$$

$$\frac{P_{\rm turb}/k_B}{10^3\,{\rm cm^{-3}\,K}} \equiv \eta_{\rm turb}\frac{\Sigma_{\rm SFR}}{10^{-3}\,M_\odot\,{\rm kpc^{-2}\,yr^{-1}}}, \qquad (21)$$

such that the yield coefficients $\eta_{\rm th}$ and $\eta_{\rm turb}$ measure the thermal and turbulent efficacies of feedback, respectively. In the analytic model for thermal/dynamical equilibrium (OML10; OS11), $\eta_{\rm th} = 1.2 f_{\rm rad}$, where $f_{\rm rad} = [0.25 + 0.75 Z'_d(\Sigma/10\,M_\odot\,{\rm pc^{-2}})^{0.4}]^{-1}$ using the heating/cooling model of Wolfire et al. (2003), and $\eta_{\rm turb} = 3.6 f_p$ for $p_*/m_* = 3000\,{\rm km\,s^{-1}}$. Our direct measurements fitting the simulation results (Equations (18) and (19)) give

$$\eta_{\rm th} = 1.3 f_{\rm rad}\left(\frac{\Sigma_{\rm SFR}}{10^{-3}\,M_\odot\,{\rm kpc^{-2}\,yr^{-1}}}\right)^{-0.14}, \qquad (22)$$

$$\eta_{\rm turb} = 4.3\left(\frac{\Sigma_{\rm SFR}}{10^{-3}\,M_\odot\,{\rm kpc^{-2}\,yr^{-1}}}\right)^{-0.11}. \qquad (23)$$

These results for yields are very close to those adopted in the analytic model, and show quite weak dependence on the SFR. For solar-neighborhood conditions, the yield coefficients are $\eta_{\rm th} = 1.1$ and $\eta_{\rm turb} = 3.9$, remarkably close to the adopted values in the analytic theory. The results from 3D models are also close to the results from the XZ models in Paper I ($\eta_{\rm th} = 0.9$ and $\eta_{\rm turb} = 3.0$ at $\Sigma_{\rm SFR} = \Sigma_{\rm SFR,0}$). In Equation (22), the control parameter for heating efficiency $f_{\rm rad}$ enters naturally into the thermal yield coefficient $\eta_{\rm th}$ since higher/lower heating efficiency (or lower/higher shielding of FUV radiation) converts more/less radiation energy from star formation feedback into

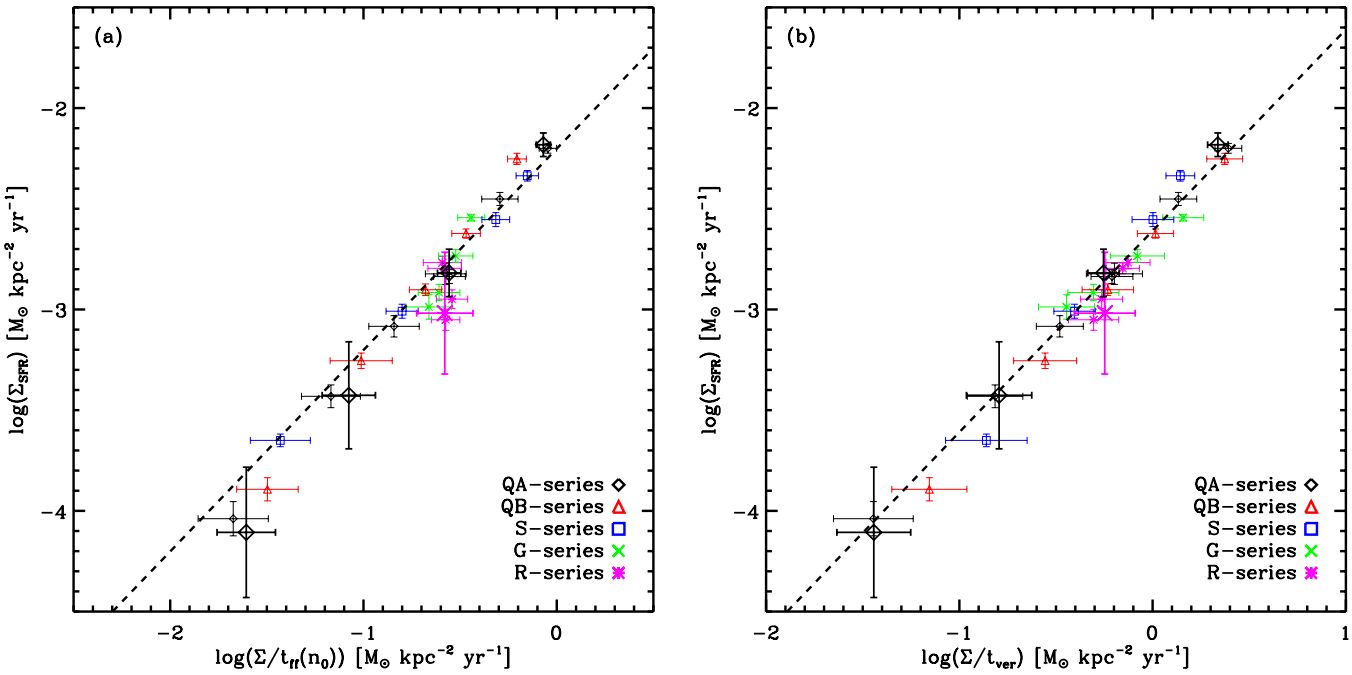

Figure 16. Measured SFR surface density $\Sigma_{\rm SFR}$ as a function of (a) $\Sigma/t_{\rm ff}(n_0)$ and (b) $\Sigma/t_{\rm ver}$ for all 3D models. The symbols have the same meanings as in Figure 11. The dashed lines in both panels are our best fits to all 3D models for an imposed unity slope, which give the coefficients of $\epsilon_{\rm ff}(n_0) = 0.006$ and $\epsilon_{\rm ver} = 0.002$.
(A color version of this figure is available in the online journal.)

thermal energy in the diffuse ISM. Although we have not directly explored variations in p_*/m_* in the present simulations (see SO12 for a study of this kind), the turbulent yield coefficient $\eta_{\rm turb}$ would be expected to vary proportional to the momentum feedback per stellar mass p_*/m_*, which would introduce an additional factor $(p_*/m_*)/3000\,{\rm km\,s^{-1}}$ to the right-hand side of Equation (23). In addition to SNe, other potential sources of momentum injection associated with star formation include radiation forces and cosmic rays (see OS11 for discussion and estimates).

The ratio of total-to-thermal pressure α can be obtained from Equations (22) and (23) as

$$\alpha = 1 + \frac{\eta_{\rm turb}}{\eta_{\rm th}} = 1 + \frac{3.1}{f_{\rm rad}}\left(\frac{\Sigma_{\rm SFR}}{10^{-3}\,M_\odot\,{\rm kpc^{-2}\,yr^{-1}}}\right)^{0.03}. \quad (24)$$

As discussed above, specific feedback momentum different from our chosen value would introduce an additional factor $(p_*/m_*)/3000\,{\rm km\,s^{-1}}$ in the second term above. For a fixed heating efficiency $f_{\rm rad}$, α is nearly constant, as seen in Figure 12(b). In the solar neighborhood ($f_{\rm rad} = 1$), $\alpha \approx 4$ is close to the fiducial value adopted by OML10 ($\alpha = 5$).

3.4. Star Formation Scaling Relations

A common characterization of the SFR is in terms of a gas mass consumption efficiency within a relevant dynamical time scale (e.g., Leroy et al. 2008 and references therein):

$$\Sigma_{\rm SFR} = \epsilon_{\rm dyn}\frac{\Sigma}{t_{\rm dyn}}. \quad (25)$$

A natural dynamical time to consider in disk galaxies is the free-fall time at the mean midplane gas density (OS11), $t_{\rm ff}(\rho_0) = [3\pi/(32G\rho_0)]^{1/2}$, where $\rho_0 = 1.4 m_p n_0$. Using the time and horizontally averaged values of ρ_0 measured in our simulations, Figure 16(a) plots our measured values of $\Sigma_{\rm SFR}$ as a function of $\Sigma/t_{\rm ff}(\rho_0)$ for all 3D models. The best fit for an imposed linear relation (dashed line) gives $\Sigma_{\rm SFR}t_{\rm ff}(\rho_0)/\Sigma \equiv \epsilon_{\rm ff}(n_0) = 0.006$. This value is close to typical values $\epsilon_{\rm ff} \sim 0.01$ inferred from observations of molecular gas (Krumholz & Tan 2007), and similar to the values for $\epsilon_{\rm ff}$ measured by SO12 in simulations of the starburst regime ($\Sigma_{\rm SFR}$ up to a few $\times\, M_\odot\,{\rm kpc^{-2}\,yr^{-1}}$).

Formation of GBCs from diffuse gas is the first step to the star formation. As described in Section 3.1, in outer disk regions where the vertical gravity from stars exceeds the (mean) vertical gravity from the gas, the initial concentration of diffuse cold cloudlets to make GBCs is primarily "falling" toward the midplane of the stellar potential. Under this circumstance, the vertical dynamical time defined by $t_{\rm ver} \equiv H_{\rm diff}/\sigma_{\rm z,diff}$ may be more relevant for gathering diffuse gas to initiate star formation than the free-fall time.[12] Using the time- and horizontally averaged values of $H_{\rm diff}$ and $\sigma_{\rm z,diff}$ defined in Section 3.2, in Figure 16(b) we plot the measured $\Sigma_{\rm SFR}$ as a function of $\Sigma/t_{\rm ver}$ for all 3D models. The dotted line denotes our best fit for an imposed unity slope, $\Sigma_{\rm SFR}t_{\rm ver}/\Sigma \equiv \epsilon_{\rm ver} = 0.002$. The free-fall time and the vertical dynamical time prescriptions give rms fractional differences between measured and estimated $\Sigma_{\rm SFR}$ of 24% and 17%, respectively.

In the theory of self-regulated star formation (OML10; OS11; Paper I), the relationships among $\Sigma_{\rm SFR}$, $P_{\rm tot}$, and $P_{\rm tot,DE}$ are key. Star formation feedback replenishes the thermal and turbulent pressures, and the total pressure supports the weight of the ISM. Figure 17(a) shows $\Sigma_{\rm SFR}$ as a function of $P_{\rm tot}$ for all 3D models. The dotted line is obtained from the sum of Equations (20) and (21) with the yield coefficients from Equations (22) and (23)

[12] Using Equation (15), $t_{\rm ver} \equiv H_{\rm diff}/\sigma_{\rm z,diff} = \Sigma_{\rm diff}\sigma_{\rm z,diff}/(\sqrt{2\pi}\,P_{\rm tot})$ in dynamical equilibrium. For diffuse-dominated regions, we therefore expect $t_{\rm ver} \approx [(\pi^3/2)^{1/2}G\Sigma/\sigma_{\rm z} + (4\pi G\rho_{\rm sd})^{1/2}]^{-1}$. In the limit that gas or stars dominates the gravity, this becomes $t_{\rm ver} \approx (\pi^2 G\rho_0)^{-1/2}$ or $t_{\rm ver} \approx (4\pi G\rho_{\rm sd})^{-1/2}$, respectively.

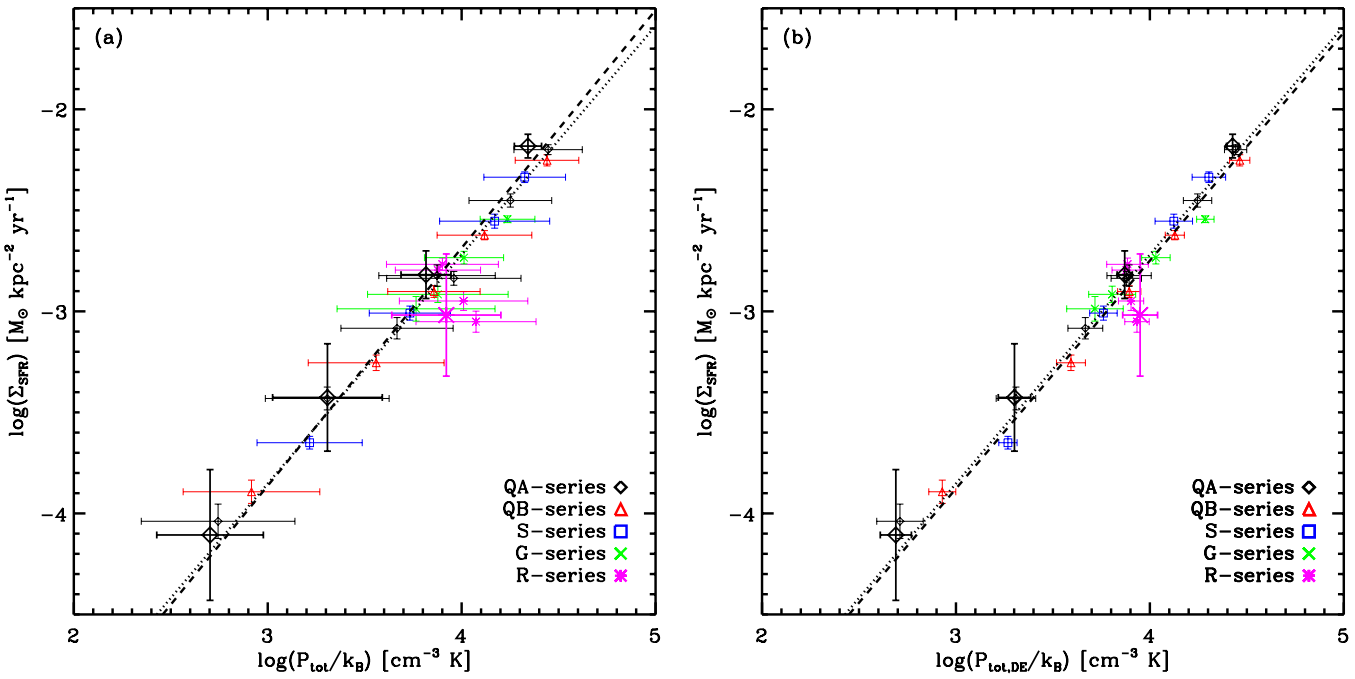

Figure 17. Measured SFR surface density $\Sigma_{\rm SFR}$ as a function of (a) the measured midplane total pressure $P_{\rm tot}$ and (b) the predicted midplane total pressure from vertical dynamical equilibrium $P_{\rm tot,DE}$. The symbols have the same meanings as in Figure 11. In both panels, the dashed line denotes our best fit (Equation (26) in (a) and Equation (27) in (b)), and the dotted line plots the predicted thermal and turbulent pressures using Equations (20) and (21) with numerically calibrated yield coefficients $\eta_{\rm th}$ (using $f_{\rm rad} = 1$) and $\eta_{\rm turb}$ from Equations (22) and (23). The higher heating efficiency $f_{\rm rad}$ in the R series results in lower $\Sigma_{\rm SFR}$ for the same $P_{\rm tot}$ by increasing $\eta_{\rm th}$, and hence η.

(A color version of this figure is available in the online journal.)

for $f_{\rm rad} = 1$, while the dashed line plots our best fit omitting the R series:

$$\Sigma_{\rm SFR} = 2.1 \times 10^{-3}\, M_\odot\,{\rm kpc}^{-2}\,{\rm yr}^{-1} \left(\frac{P_{\rm tot}/k_{\rm B}}{10^4\,{\rm cm}^{-3}\,{\rm K}}\right)^{1.18}. \quad (26)$$

Since both thermal and turbulent pressures separately satisfy nearly linear relationships with $\Sigma_{\rm SFR}$ as shown in Section 3.3, the dotted and dashed lines agree very well with each other. Note that the proportionality constant in the above relation for $\Sigma_{\rm SFR}$ versus $P_{\rm tot}$ is roughly $4(p_*/m_*)^{-1}$, showing that the specific momentum injected by SNe determines the coefficient of the $\Sigma_{\rm SFR}$–$P_{\rm tot}$ relation.

From Equations (22) and (23), we obtain the total feedback yield $\eta \equiv \eta_{\rm th} + \eta_{\rm turb}$, which includes the effect of $f_{\rm rad}$. In regions of higher heating efficiency (or lower shielding), the thermal feedback yield (and hence total feedback yield) increases. The points from the R series in Figure 17 (magenta asterisks) thus spread vertically with respect to model QA10.

In addition to the near-linear relationship between $\Sigma_{\rm SFR}$ and $P_{\rm tot}$ arising from the balance between energy gains and losses, the separate relation $P_{\rm tot} = P_{\rm tot,DE}$ holds due to vertical dynamical equilibrium (Section 3.3). We thus can obtain a similar relation between $\Sigma_{\rm SFR}$ and $P_{\rm tot,DE}$, as shown in Figure 17(b). Our best fit analogous to Equation (26) is

$$\Sigma_{\rm SFR} = 1.8 \times 10^{-3}\, M_\odot\,{\rm kpc}^{-2}\,{\rm yr}^{-1} \left(\frac{P_{\rm tot,DE}/k_{\rm B}}{10^4\,{\rm cm}^{-3}\,{\rm K}}\right)^{1.13}. \quad (27)$$

This relation provides a prediction for $\Sigma_{\rm SFR}$ in simultaneous thermal and dynamical equilibrium, based only (via Equation (15) with $f_{\rm diff} \sim 1$) on the total gas surface density and stellar/dark matter density present at a given location in a galactic disk.

We remark that the "dynamical time" formulation of the SFR is in fact related to the thermal/dynamical equilibrium formulation (based on momentum flux matching), but the latter is more fundamental. Considering the turbulence-dominated case, balancing momentum flux requires $\rho_0 v_{\rm z,diff}^2 \approx (1/4)(p_*/m_*)\Sigma_{\rm SFR}$. Using $\rho_0 v_{\rm z,diff}^2 = v_{\rm z,diff}\Sigma_{\rm diff} \times v_{\rm z,diff}/(\sqrt{2\pi}H_{\rm diff})$, this can be interpreted physically as the statement that the dissipation of momentum on a vertical crossing time $\sim v_{\rm z,diff}\Sigma_{\rm diff} \times (v_{\rm z,diff}/H)$ must be balanced by injection of fresh momentum by star formation $\sim(p_*/m_*)\Sigma_{\rm SFR}$. The momentum balance formula may be re-expressed as $\Sigma_{\rm SFR}(\Sigma_{\rm diff}/t_{\rm ver})^{-1} \equiv \epsilon_{\rm ver} = v_{\rm z,diff}[(1/4) f_p \sqrt{2\pi}\, p_*/m_*]^{-1}$. A relationship of the form in Equation (25) for $t_{\rm dyn} = t_{\rm ver}$ then holds provided that $v_{\rm z,diff}$ is constant. From this point of view, the low rate of "gas consumption" relative to the vertical dynamical time reflects the "inefficiency" of converting ordered feedback momentum injected on a small scale to a pervasive turbulent velocity dispersion on scales comparable to the disk thickness. That is, $\epsilon_{\rm ver}$ (or $\epsilon_{\rm ff}$) is small because $v_{\rm z,diff}[(1/4)\sqrt{2\pi}\, p_*/m_*]^{-1}$ is small. Alternatively, the kinetic energy injected to the ISM by each feedback event, $\sim p_* v_{\rm z,diff}$, is large compared to the kinetic energy lost from the ISM, $\sim v_{\rm z,diff}^2 m_*$, when gas is locked up in stars leading up to the feedback event. In contrast, the efficiency of *momentum* replenishment per dynamical time is order-unity.

In conclusion, we find that a nearly linear relationship between $\Sigma_{\rm SFR}$ and $P_{\rm tot,DE}$ is strongly supported by our numerical simulations. Depending on whether stars or gas dominate the local vertical potential well, this would lead to either a relation $\Sigma_{\rm SFR} \propto \Sigma\sqrt{\rho_{\rm sd}}$ (typically outer disks, as modeled here and in Paper I) or $\Sigma_{\rm SFR} \propto \Sigma^2$ (typically starburst regions, as modeled by OS11 and SO12). An increase in either the heating efficiency

or the turbulent driving efficiency would tend to lower $\Sigma_{\rm SFR}$ for given values of the gas and stellar disk parameters Σ and $\rho_{\rm sd}$.

4. SUMMARY AND DISCUSSION

In this paper, we have carried out full 3D simulations of the turbulent, multiphase ISM in galactic disks, including the physical effects from galactic differential rotation, gaseous self-gravity, vertical gravity due to stars and dark matter, and cooling and heating as appropriate for atomic gas. We also incorporate thermal and kinetic feedback tied to recent star formation, via a time-dependent heating rate coefficient and turbulent driving from expanding SN remnants.

We use our simulations to investigate the relationships between ISM properties and SFRs, and we also compare our numerical results to the predictions of a recent theory for thermal/dynamical equilibrium of the ISM and self-regulated star formation (OML10; OS11). The theory posits that the rate of star formation adjusts until the total energy (in turbulent driving and thermal heating) supplied to the ISM by star formation feedback matches the demand imposed by ISM losses (turbulence dissipation and interstellar cooling). Force balance must also hold: the momentum flux (thermal and turbulent) provided by feedback must match the vertical weight of the ISM in the total gravitational field (gas, stellar, and dark matter gravity). Our simulations provide quantitative evidence in support of the theory. This confirms our previous results (Paper I) based on radial-vertical simulations in the same atomic-dominated regime, together with the simulations of SO12 for the molecular-dominated starburst regime.

Our main findings are summarized as follows.

1. *Vertical support of the disk.* Despite large amplitude temporal fluctuations, we find that the mean total (thermal *plus* turbulent) midplane pressure $P_{\rm tot}$ matches the mean vertical weight of the gas ($P_{\rm tot,DE}$, as defined in Equation (15)) within 12%. Vertical dynamical equilibrium in the highly turbulent, multiphase ISM has also previously been demonstrated in simulations with a range of sources of turbulence: expansion of H II regions (Koyama & Ostriker 2009b), magnetorotational instability (Piontek & Ostriker 2007), galactic spiral shocks (Kim et al. 2010), and SN feedback (Paper I; SO12; Hill et al. 2012). These numerical results support the assumption of effective "hydrostatic" equilibrium that is often utilized in observations to obtain an estimate of the midplane pressure (Wong & Blitz 2002; Blitz & Rosolowsky 2004, 2006; Leroy et al. 2008). Equation (15) provides a general expression for the pressure under vertical dynamical equilibrium. When the vertical gravity is dominated by stars and dark matter, as in the outer regions of disk galaxies or dwarf galaxies, Equation (16) gives $P_{\rm tot,DE} \propto \Sigma\sqrt{\rho_{\rm sd}}$, while $P_{\rm tot,DE} \propto \Sigma^2$ if gaseous self-gravity dominates—typically in starbursts (OS11; SO12).
2. *Thermal and turbulent energy replenishment from star formation feedback.* Since turbulence decays within a flow crossing time (Stone et al. 1998; Mac Low et al. 1998; comparable to the vertical dynamical time $t_{\rm ver} = H/v_z$ for the neutral ISM disk) and the cooling time of the atomic gas is even shorter than this dynamical time, both turbulent driving and heating are required to maintain the quasi-steady state over a few orbital times that appears to hold in normal disk galaxies. Without continuous turbulent driving and heating, the gas disk would rapidly collapse, leading to unrealistically high $\Sigma_{\rm SFR}$ (e.g., Dobbs et al. 2011; Hopkins et al. 2011). In our simulations, star formation feedback modeling SN explosions and photoelectric heating by FUV radiation replenishes the turbulent and thermal energies at a rate $\propto \Sigma_{\rm SFR}$. For a given gas surface density Σ, the cooling and turbulent dissipation rates per unit mass increase when the gas disk's scale height decreases, because the volume density ρ increases. However, higher ρ also leads to more rapid gravitational collapse and an increase in $\Sigma_{\rm SFR}/\Sigma$. The SFR can therefore adjust to meet the ISM's demands for energy inputs.

   In the OML10 theory, the demand to maintain thermal balance in multiphase atomic ISM translates to the requirement that the thermal pressure at the midplane $P_{\rm th}$ should lie between the maximum pressure of the warm phase $P_{\rm max}$ and the minimum pressure of the cold phase $P_{\rm min}$ (Field et al. 1969; Wolfire et al. 1995, 2003). Here, we have compared the measured $P_{\rm th}$ to the geometric-mean pressure $P_{\rm two} \equiv (P_{\rm min}P_{\rm max})^{1/2} \propto \Sigma_{\rm SFR}$, showing that $P_{\rm th} \approx P_{\rm two}$ indeed holds with weak decreasing trend toward increasing $\Sigma_{\rm SFR}$. The variation of $P_{\rm th}/P_{\rm two}$ is only $\sim$0.4 dex for two orders of magnitude change in $\Sigma_{\rm SFR}$ and the measured $P_{\rm th}$. This confirms both the hypothesis of OML10 and our previous numerical results from Paper I.

   In OS11 (see also Paper I and SO12), it is shown that the demand to offset turbulent dissipation with turbulent driving from star formation feedback translates to the requirement that $P_{\rm turb} = \rho v_z^2 \sim \Sigma v_z/t_{\rm ver}$ is comparable to $P_{\rm driv} \equiv (1/4)(p_*/m_*)\Sigma_{\rm SFR}$. Here, we have compared the measured $P_{\rm turb}$ to $P_{\rm driv}$, showing that $P_{\rm turb} \approx P_{\rm driv}$ holds, again with a weak decreasing trend as $\Sigma_{\rm SFR}$ increases. Similar to $P_{\rm th}/P_{\rm two}$, $P_{\rm turb}/P_{\rm driv}$ varies only over $\sim$0.3 dex for two orders of magnitude change in $\Sigma_{\rm SFR}$ and the measured $P_{\rm turb}$. This confirms the hypothesis of OS11 and our previous findings from XZ simulations (Paper I), as well as numerical results of SO12 for the starburst regime, in which turbulent pressure is completely dominant over other pressures.

3. *Thermal and turbulent energy yields.* The equilibrium pressures depend on a balance between losses and gains: $P_{\rm turb}/t_{\rm ver} \sim$ (turbulent energy driving/volume/time) $\sim (v_z/H)\times$ (turbulent momentum driving/area/time) so that $P_{\rm turb} = f_p(1/4)(p_*/m_*)\Sigma_{\rm SFR}$ in equilibrium; and $P_{\rm th}/t_{\rm cool} \sim$ (thermal heating/volume/time) so that $P_{\rm th} = \Gamma k_{\rm B}T/\Lambda(T) \propto f_{\rm rad}\Sigma_{\rm SFR}$ in equilibrium. We quantify the results in terms of feedback yield parameters $\eta_{\rm th}$ and $\eta_{\rm turb}$, corresponding to the ratio $P_{\rm th}/\Sigma_{\rm SFR}$ and $P_{\rm turb}/\Sigma_{\rm SFR}$, respectively, in suitable units (see Equations (20) and (21)). We find that $\eta_{\rm th}$ and $\eta_{\rm turb}$ are nearly constant (see Equations (22) and (23)) in our models with $f_{\rm rad} = 1$. Thus, even though $\Sigma_{\rm SFR}$ and the individual thermal and turbulent pressures vary over two orders of magnitude, the ratio of the total-to-thermal pressure $\alpha = 1 + \eta_{\rm turb}/\eta_{\rm th} \sim$ 4–5 is nearly constant (see Figure 12). From the above, the ratio $P_{\rm turb}/P_{\rm th}$ is approximately equal to the product of $t_{\rm ver}/t_{\rm cool}$ and $\dot{\mathcal{E}}_{\rm turb}/\dot{\mathcal{E}}_{\rm th}$. Although the input rate of turbulent energy $\dot{\mathcal{E}}_{\rm turb}$ is small compared to the input rate of thermal energy $\dot{\mathcal{E}}_{\rm th}$ ($\sim$4% for the solar neighborhood), $t_{\rm ver}$ is much larger than $t_{\rm cool}$ (by a factor $\sim$100 for the solar neighborhood), so that the resulting $P_{\rm turb}$ exceeds $P_{\rm th}$. Since the dependence $t_{\rm ver}/t_{\rm cool} \propto \Sigma$ is compensated by $\dot{\mathcal{E}}_{\rm turb}/\dot{\mathcal{E}}_{\rm th} \propto \Sigma^{-1}$, the ratio $P_{\rm turb}/P_{\rm th}$ can remain roughly the same over a large range of radii in disks.

The feedback yield increases if either the parameters governing gains increase or those governing losses decrease. The heating rate in our models is $\propto f_{\rm rad}\Sigma_{\rm SFR}$. Because Γ is expected to be proportional to dust abundance for photoelectric heating and Λ is expected to be proportional to metal abundance for C or O cooling, these dependences would roughly cancel in $\eta_{\rm th}$ if dust and metals vary together. However, the heating rate for a given $\Sigma_{\rm SFR}$ is expected to increase in low-A_V regions of galaxies where FUV radiation can propagate farther (see OML10); we explore this effect via varying $f_{\rm rad}$. Our models show that $\eta_{\rm th}$ increases with $f_{\rm rad}$, consistent with expectations. As explicitly explored in SO12 and expected from our result $P_{\rm turb}/P_{\rm driv} \sim 1$, $\eta_{\rm turb}$ depends nearly linearly on p_*/m_*. In the present simulations, the value of $p_*/m_* = 3000\,{\rm km\,s^{-1}}$ we adopt is based on the value of p_* for a radiative-stage spherical SN remnant propagating into a uniform medium (Cioffi et al. 1988; Blondin et al. 1998; Thornton et al. 1998). SNe are expected to be the dominant source of turbulence in the diffuse ISM in many cases (see Mac Low & Klessen 2004; OS11), but p_* may still vary and it is important to calibrate this parameter via high-resolution simulations of a realistic (cloudy) ISM. Although $\eta_{\rm turb}$ exceeds $\eta_{\rm th}$ for the parameter sets we have explored, potentially the reverse situation could hold in some galactic environments.

4. *A link between SFR and disk properties.* Given basic disk properties (the total gas surface density Σ and stellar+dark matter density $\rho_{\rm sd}$), a theory of large-scale star formation should be able to provide a prediction for $\Sigma_{\rm SFR}$. In the OML10+OS11 model, this prediction is obtained by requiring that thermal and turbulent balance equations hold, and also that vertical pressure/gravity balance holds. Simultaneous solution of these three balance equations leads to the result that $\Sigma_{\rm SFR}$ varies nearly linearly with $P_{\rm tot,DE}$ (as defined in Equation (15); $f_{\rm diff} \sim 1$ for the regime studied here). We verify this result with our simulations, as seen in Figure 17 and Equation (27). Depending on whether the gas gravity or the gravity of the stars dominates in Equation (15), this can lead to $\Sigma_{\rm SFR} \propto \Sigma^2$ for starburst systems (OS11; SO12), or to $\Sigma_{\rm SFR} \propto \Sigma\sqrt{\rho_{\rm sd}}$ for normal outer disk regions (OML10; Paper I).

   In recent local observations of the $\Sigma_{\rm SFR}$ versus Σ relation, the low-Σ regime is characterized by large scatter of composite data sets (Bigiel et al. 2008) and systematic differences in power-law indices p in $\Sigma_{\rm SFR} \propto \Sigma^{1+p}$ between individual galaxies (Wong & Blitz 2002; Leroy et al. 2008). Our simulations suggest that this may, in part, be due to "projection" on the $\Sigma_{\rm SFR}$ versus Σ plane that neglects variations in the gravity of the stellar disk (which would lead to $\Sigma_{\rm SFR} \propto \sqrt{\rho_{\rm sd}}$). In fact, Blitz & Rosolowsky (2006) and Leroy et al. (2008) have demonstrated that molecular content and the SFR increase with increasing stellar density. In Paper I (see Figure 13(a) there), we showed that $\Sigma_{\rm SFR}$ at a given Σ moves up or down when the ratio of external (stellar) gravity to gas gravity (controlled by $1/s_0$) is varied. Our current simulations show the same effect. In the particular case where stellar and gaseous Q values are constant (QA and QB series), $\sqrt{\rho_{\rm sd}} \propto \Sigma$, which would lead to a steep relation $\Sigma_{\rm SFR} \propto \Sigma^2$.

   We show in Section 3.4 that dynamical time prescriptions are also good descriptions of our numerical results; we find $\Sigma_{\rm SFR} = 0.006\Sigma/t_{\rm ff}(\rho_0)$ and $\Sigma_{\rm SFR} = 0.002\Sigma/t_{\rm ver}$. However, we argue that the relation between pressure and SFR is more fundamental and direct than these dynamical time prescriptions. The relation $\Sigma_{\rm SFR} \propto P_{\rm tot,DE}$ requires that p_*/m_* is approximately constant, whereas $\Sigma_{\rm SFR} \propto \Sigma/t_{\rm ver}$ requires that $v_z(p_*/m_*)^{-1}$ is approximately constant, and $\Sigma_{\rm SFR} \propto \Sigma/t_{\rm ff}$ requires that $v_z(g_z/G\Sigma)^{1/2}(p_*/m_*)^{-1}$ is approximately constant. Our simulations (as well as others; see below) do find approximately constant turbulent velocity dispersions v_z. The family of simulations we conducted also happens to have $g_z/G\Sigma$ constant because $g_z \sim (G\rho_{\rm sd})^{1/2}v_z$ and we adopted $\rho_{\rm sd} \propto \Sigma^2$. When gas dominates the vertical gravity (as in starburst regions), $g_z \sim G\Sigma$, which combined with constant v_z results in $\Sigma_{\rm SFR} \propto \Sigma/t_{\rm ff}$ as shown in SO12; however, this need not be the case for galaxies in general.

   The present models focus on the ISM regime in which diffuse gas dominates—i.e., outer disks at low gas surface density Σ. Moving to smaller radii and regions of higher surface density, observations (e.g., Bigiel et al. 2008; Leroy et al. 2008) show that gas in gravitationally bound molecular clouds exceeds the diffuse atomic gas, and that $\Sigma_{\rm SFR} \propto \Sigma$ with little dependence on $\rho_{\rm sd}$. One interpretation of the transition from outer disks to these mid-disk regions is that it represents an increase of $t_{\rm dest}/t_{\rm form}$ from small to large values, where these timescales represent formation and destruction timescales for GBCs. If formation and destruction are in balance, then we expect $f_{\rm diff} = t_{\rm form}/(t_{\rm form} + t_{\rm dest})$. Dynamical equilibrium between pressure and gravity in the diffuse ISM requires $\eta\Sigma_{\rm SFR} \sim f_{\rm diff}\Sigma g_z \sim \Sigma g_z t_{\rm form}/(t_{\rm form} + t_{\rm dest})$. If $t_{\rm form} \sim t_{\rm ver}$, then $g_z t_{\rm form} \sim v_z$. Furthermore, if v_z and $t_{\rm dest}$ are roughly constant (and $t_{\rm form} \ll t_{\rm dest}$), this would lead to $f_{\rm diff} \ll 1$ and $\Sigma_{\rm SFR} \propto \Sigma$. Testing whether this or another interpretation explains mid-disk observations will require detailed models of cloud destruction, carefully following feedback processes throughout the lives of massive stars.

5. *Velocity dispersion driven by star formation feedback.* Balance between turbulent driving and dissipation leads to $v_{z,\rm diff} = (\sqrt{2\pi}/4) f_p (p_*/m_*)\Sigma_{\rm SFR}(\Sigma/t_{\rm ver})^{-1}$. If star formation scales as $\Sigma_{\rm SFR} = \epsilon_{\rm ver}\Sigma/t_{\rm ver}$ (see Section 3.4), this yields $v_{z,\rm diff} = 0.63 f_p \epsilon_{\rm ver}(p_*/m_*) \sim 3.8$–$5.6\,{\rm km\,s^{-1}}$ for $\epsilon_{\rm ver} = 0.2\%$, $f_p = 1$–1.5, and $p_*/m_* = 3000\,{\rm km\,s^{-1}}$, insensitive to Σ, $\rho_{\rm sd}$, and $\Sigma_{\rm SFR}$. The measured values of turbulent velocity dispersion in our simulations are more or less constant over the whole range of parameters (see Figure 11) since f_p depends very weakly on $\Sigma_{\rm SFR}$ (see Figure 15 and Equation (19)). Many other recent simulations have also found nearly constant velocity dispersions with respect to the input SFR (e.g., Dib et al. 2006; Shetty & Ostriker 2008; Agertz et al. 2009; Joung et al. 2009; Dobbs et al. 2011; SO12). H I velocity dispersions reported in observations of the Milky Way and nearby face-on galaxies (Dickey et al. 1990; van Zee & Bryant 1999; Heiles & Troland 2003; Petric & Rupen 2007; Kalberla & Kerp 2009) show comparable values and insensitivity to the $\Sigma_{\rm SFR}$. Variations in the turbulent velocity amplitude driven by feedback could arise, however, if p_*/m_* differs in more extreme environments.

   Although turbulence driven by feedback appears to be crucial in preventing runaway star formation, other mechanisms can also help to drive ISM turbulence. These mechanisms include unsteady galactic spiral shocks (Kim & Ostriker 2006; Kim et al. 2006, 2010; Dobbs & Bonnell 2006), magnetorotational instability (Kim et al. 2003;

Piontek & Ostriker 2005, 2007), large-scale gravitational instabilities (Wada & Norman 2002; Kim & Ostriker 2007; Agertz et al. 2009; Bournaud et al. 2010), and cosmic inflow (Klessen & Hennebelle 2010). Large-scale gravitational instabilities may be particularly important in driving non-circular motions in ultraluminous infrared galaxies and high-redshift galaxies, where measured velocity dispersions appear larger than in local disks (see, e.g., Figure 14 of Genzel et al. 2011). However, it is important to keep in mind that force balance in the vertical direction depends on velocity dispersions at scales below the disk thickness (much smaller than has been resolved in external galaxies), whereas gravitational instabilities primarily drive turbulence at scales larger than the disk thickness. Turbulence driven by any of these mechanisms at scales smaller than the disk thickness would tend to reduce the SFR, since it would partially offset the demand for star formation feedback to match the required pressure. Magnetic fields also contribute pressure, but because the magnitude is smaller than turbulent pressure and the magnetic scale height is large, the fractional contribution to offsetting the weight of the neutral ISM is small (OS11; Hill et al. 2012). In future models, it will be interesting to quantify both how important various sources (including diverse feedback processes) are for driving turbulent velocity dispersions in the ISM, and the corresponding effects on limiting star formation.

We are grateful to the referee for a helpful review. This work was made possible by the facilities of the Shared Hierarchical Academic Research Computing Network (SHARCNET: www.sharcnet.ca) and Compute/Calcul Canada. Part of the numerical simulations were performed by using a high performance computing cluster in the Korea Astronomy and Space Science Institute. The work of C.-G.K. was supported in part by a CITA National Fellowship. The work of E.C.O. was supported by grant AST0908185 from the National Science Foundation. The work of W.-T.K. was supported by the National Research Foundation of Korea (NRF) grant funded by the Korean government (MEST), No. 2010-0000712.

REFERENCES

Agertz, O., Kravtsov, A. V., Leitner, S. N., & Gnedin, N. Y. 2013, ApJ, 770, 25
Agertz, O., Lake, G., Teyssier, R., et al. 2009, MNRAS, 392, 294
Bakes, E. L. O., & Tielens, A. G. G. M. 1994, ApJ, 427, 822
Bigiel, F., Leroy, A., Walter, F., et al. 2008, AJ, 136, 2846
Blitz, L., & Rosolowsky, E. 2004, ApJL, 612, L29
Blitz, L., & Rosolowsky, E. 2006, ApJ, 650, 933
Blondin, J. M., Wright, E. B., Borkowski, K. J., & Reynolds, S. P. 1998, ApJ, 500, 342
Bournaud, F., Elmegreen, B. G., Teyssier, R., Block, D. L., & Puerari, I. 2010, MNRAS, 409, 1088
Cioffi, D. F., McKee, C. F., & Bertschinger, E. 1988, ApJ, 334, 252
Cox, D. P. 2005, ARA&A, 43, 337
Dib, S., Bell, E., & Burkert, A. 2006, ApJ, 638, 797
Dickey, J. M., Hanson, M. M., & Helou, G. 1990, ApJ, 352, 522
Dickey, J. M., Strasser, S., Gaensler, B. M., et al. 2009, ApJ, 693, 1250
Dobbs, C. L., & Bonnell, I. A. 2006, MNRAS, 367, 873
Dobbs, C. L., Burkert, A., & Pringle, J. E. 2011, MNRAS, 417, 1318
Elmegreen, B. G., & Scalo, J. 2004, ARA&A, 42, 211
Ferrière, K. M. 2001, RvMP, 73, 1031
Field, G. B., Goldsmith, D. W., & Habing, H. J. 1969, ApJL, 155, L149
Fuchs, B., Jahreiß, H., & Flynn, C. 2009, AJ, 137, 266
Gammie, C. F. 2001, ApJ, 553, 174
Gazol, A., & Kim, J. 2013, ApJ, 765, 49
Gazol, A., Luis, L., & Kim, J. 2009, ApJ, 693, 656
Gazol, A., Vázquez-Semadeni, E., & Kim, J. 2005, ApJ, 630, 911
Genzel, R., Newman, S., Jones, T., et al. 2011, ApJ, 733, 101
Heiles, C., & Troland, T. H. 2003, ApJ, 586, 1067
Hill, A. S., Joung, M. R., Mac Low, M.-M., et al. 2012, ApJ, 750, 104
Hopkins, P. F., Quataert, E., & Murray, N. 2011, MNRAS, 417, 950
Joung, M. R., Mac Low, M., & Bryan, G. L. 2009, ApJ, 704, 137
Kalberla, P. M. W., & Kerp, J. 2009, ARA&A, 47, 27
Kim, C.-G., Kim, W.-T., & Ostriker, E. C. 2006, ApJL, 649, L13
Kim, C.-G., Kim, W.-T., & Ostriker, E. C. 2010, ApJ, 720, 1454
Kim, C.-G., Kim, W.-T., & Ostriker, E. C. 2011, ApJ, 743, 25 (Paper I)
Kim, W.-T., & Ostriker, E. C. 2001, ApJ, 559, 70
Kim, W.-T., & Ostriker, E. C. 2006, ApJ, 646, 213
Kim, W.-T., & Ostriker, E. C. 2007, ApJ, 660, 1232
Kim, W.-T., Ostriker, E. C., & Stone, J. M. 2002, ApJ, 581, 1080
Kim, W.-T., Ostriker, E. C., & Stone, J. M. 2003, ApJ, 599, 1157
Klessen, R. S., & Hennebelle, P. 2010, A&A, 520, A17
Koo, B., & Kang, J. 2004, MNRAS, 349, 983
Koyama, H., & Inutsuka, S. 2002, ApJL, 564, L97
Koyama, H., & Ostriker, E. C. 2009a, ApJ, 693, 1316
Koyama, H., & Ostriker, E. C. 2009b, ApJ, 693, 1346
Kroupa, P. 2001, MNRAS, 322, 231
Krumholz, M. R., Dekel, A., & McKee, C. F. 2012, ApJ, 745, 69
Krumholz, M. R., & McKee, C. F. 2005, ApJ, 630, 250
Krumholz, M. R., & Tan, J. C. 2007, ApJ, 654, 304
Leroy, A. K., Walter, F., Brinks, E., et al. 2008, AJ, 136, 2782
Lockman, F. J., & Gehman, C. S. 1991, ApJ, 382, 182
Mac Low, M., & Klessen, R. S. 2004, RvMP, 76, 125
Mac Low, M., Klessen, R. S., Burkert, A., & Smith, M. D. 1998, PhRvL, 80, 2754
Mac Low, M.-M. 1999, ApJ, 524, 169
McKee, C. F., & Ostriker, J. P. 1977, ApJ, 218, 148
Ostriker, E. C., McKee, C. F., & Leroy, A. K. 2010, ApJ, 721, 975 (OML10)
Ostriker, E. C., & Shetty, R. 2011, ApJ, 731, 41 (OS11)
Parravano, A., Hollenbach, D. J., & McKee, C. F. 2003, ApJ, 584, 797
Petric, A. O., & Rupen, M. P. 2007, AJ, 134, 1952
Pineda, J. L., Langer, W. D., Velusamy, T., & Goldsmith, P. F. 2013, A&A, 554, A103
Piontek, R. A., & Ostriker, E. C. 2004, ApJ, 601, 905
Piontek, R. A., & Ostriker, E. C. 2005, ApJ, 629, 849
Piontek, R. A., & Ostriker, E. C. 2007, ApJ, 663, 183
Saury, E., Miville-Deschênes, M.-A., Hennebelle, P., Audit, E., & Schmidt, W. 2013, arXiv:1301.3446
Seo, W.-Y., & Kim, W.-T. 2013, ApJ, 769, 100
Shetty, R., & Ostriker, E. C. 2008, ApJ, 684, 978
Shetty, R., & Ostriker, E. C. 2012, ApJ, 754, 2 (SO12)
Sternberg, A., McKee, C. F., & Wolfire, M. G. 2002, ApJS, 143, 419
Stone, J. M., & Gardiner, T. 2009, NewA, 14, 139
Stone, J. M., & Gardiner, T. A. 2010, ApJS, 189, 142
Stone, J. M., Ostriker, E. C., & Gammie, C. F. 1998, ApJL, 508, L99
Thornton, K., Gaudlitz, M., Janka, H.-T., & Steinmetz, M. 1998, ApJ, 500, 95
Truelove, J. K., Klein, R. I., McKee, C. F., et al. 1997, ApJL, 489, L179
van Zee, L., & Bryant, J. 1999, AJ, 118, 2172
Wada, K., & Norman, C. A. 2002, ApJL, 566, L21
Wolfire, M. G., Hollenbach, D., McKee, C. F., Tielens, A. G. G. M., & Bakes, E. L. O. 1995, ApJ, 443, 152
Wolfire, M. G., McKee, C. F., Hollenbach, D., & Tielens, A. G. G. M. 2003, ApJ, 587, 278
Wong, T., & Blitz, L. 2002, ApJ, 569, 157